April 1991 • SERI/TP-214-4271

PROPERTY OF
U. S. GOVERNMENT

Research on Stable, High-Efficiency Amorphous Silicon Multijunction Modules

Semiannual Subcontract Report
Phase 1: 1 May 1990 - 31 October 1990

SOLAR ENERGY RESEARCH INSTITUTE
TECHNICAL LIBRARY

MAY 23 1991

GOLDEN, COLORADO 80401

A. Catalano, R. Arya, M. Bennett, B. Fieselmann, Y. Li, J. Morris, J. Newton, R. Podlesny, S. Wiedeman, L. Yang
Solarex Thin Film Division
Newtown, Pennsylvania

lar Energy Research Institute
division of Midwest Research Institute
erated for the U.S. Department of Energy
der contract No. DE-AC02-83CH10093

SERI/TP-214-4271 c.2

SERI/TP-214-4271 • UC Category: 271 • DE91002138

SERI/TP--214-4271

DE91 002138

Research on Stable, High-Efficiency Amorphous Silicon Multijunction Modules

Semiannual Subcontract Report
Phase 1: 1 May 1990 - 31 October 1990

A. Catalano, R. Arya, M. Bennett,
B. Fieselmann, Y. Li, J. Morris,
J. Newton, R. Podlesny, S. Wiedeman,
L. Yang
Solarex Thin Film Division
Newtown Pennsylvania

SERI technical monitor: W. Luft

Solar Energy Research Institute
1617 Cole Boulevard
Golden, Colorado 80401-3393
A Division of Midwest Research Institute
Operated for the U.S. Department of Energy
under Contract No. DE-AC02-83CH10093

Prepared under Subcontract No. ZM-0-19033-1

April 1991

MASTER

DISTRIBUTION OF THIS DOCUMENT IS UNLIMITED

This publication was reproduced from the best available camera-ready copy submitted by the subcontractor and received no editorial review at SERI.

NOTICE

This report was prepared as an account of work sponsored by an agency of the United States government. Neither the United States government nor any agency thereof, nor any of their employees, makes any warranty, express or implied, or assumes any legal liability or responsibility for the accuracy, completeness, or usefulness of any information, apparatus, product, or process disclosed, or represents that its use would not infringe privately owned rights. Reference herein to any specific commercial product, process, or service by trade name, trademark, manufacturer, or otherwise does not necessarily constitute or imply its endorsement, recommendation, or favoring by the United States government or any agency thereof. The views and opinions of authors expressed herein do not necessarily state or reflect those of the United States government or any agency thereof.

Printed in the United States of America
Available from:
National Technical Information Service
U.S. Department of Commerce
5285 Port Royal Road
Springfield, VA 22161

Price: Microfiche A01
Printed Copy A04

Codes are used for pricing all publications. The code is determined by the number of pages in the publication. Information pertaining to the pricing codes can be found in the current issue of the following publications which are generally available in most libraries: *Energy Research Abstracts (ERA)*; *Government Reports Announcements* and Index (*GRA* and I); *Scientific and Technical Abstract Reports (STAR)*; and publication NTIS-PR-360 available from NTIS at the above address.

SUMMARY

Goal: The primary goal of the Phase I effort is to demonstrate a multi-junction module with a stabilized efficiency of ≥ 8.8%.

Semiconductor Materials and Device Research

Higher quality a-SiGe:H devices are necessary to achieve improved multi-junction performance. As part of the effort to prepare low bandgap alloys with improved transport properties, we have undertaken a study of the consequences of hydrogen dilution on atomic structure and on both photoconductivity and diffusion length. In particular, the effect of H-dilution on the extent of SiH_n and GeH_n bonding was investigated. It is clear from these studies that adding even small amounts of GeH_4 to an SiH_4-only discharge results in a marked increase in the number of SiH_2 bonds. H-dilution of 5:1 and 20:1 reduce the concentration of SiH_2 bonds. Both the minority (hole) and electron transport properties are improved substantially by this method, although there is still a diminution of properties with added GeH_4.

Pure a-Ge:H films were also prepared by rf and d.c. glow discharge to see if the promising results obtained recently by the Harvard group (1) could be utilized in devices. We failed to see a large difference in properties of films deposited at powered and unpowered electrodes, nor did we see as large a diffusion length as measured on samples prepared by the Harvard group. Films prepared on the cathode by the d.c. method do show some improvement over films grown on the anode.

We, and others, rely heavily on transport and optical properties of i-layer films to draw conclusions on the efficacy of preparation conditions on film properties. We have noted that the thickness of the films used in measurements has a marked effect on the apparent quality of the films, with the thicker films generally having the best transport properties. An analysis has been performed and is discussed which shows that the thickness dependence can be entirely explained by surface recombination. This may account for the different values reported by various laboratories for films prepared under nominally identical conditions.

An "ad hoc" model for the degradation of triple junction devices has been developed based on the measured behavior of single junction a-Si:H and a-SiGe:H devices. The model uses as input the degradation temperature, i-layer thickness and optical bandgap to calculate the time dependent performance of the resulting device. A semilogarithmic dependence on time, observed for single junction devices, holds for the multijunction devices. In a-Si:H/a-Si:H/a-SiGe:H devices, where

proper current balance can only be achieved when the thickness of the i_2 layer is the greatest, the thickness of this layer dominates the stability, and the rate of fall-off of performance increases linearly with thickness.

It has also been found that increasing temperature markedly reduces the rate of degradation of cells and that the optical bandgap of the (usually) very thin bottom a-SiGe:H cell has little influence on light degradation. Good agreement of the model with experiment has been obtained. Devices with a 9.6% initial efficiency which degrade 10% in 1000 hours have been tested.

Microcrystalline films have been prepared by the rapid thermal anneal of a-Si:H films. Very high conductivity p-layers have been obtained by this method. However, devices fabricated on such films have not yet shown satisfactory performance, despite attempts to chemically remove possible contamination at the p/i interface.

Non-Semiconductor Materials Research

Previous analysis has shown that major optical losses occur at both front and rear electrical contacts. To address these losses, we have sought to develop an improved transparent front contact material as well as a more highly reflecting transparent rear contact. Both ZnO and SnO_2 are being developed for the front contact, while ZnO is being pursued as an alternative to ITO for the rear contact.

For the front contact, which is deposited on glass, atmospheric, as well as low pressure CVD of ZnO, have been performed. Preliminary experiments conducted in a batch mode experienced difficulty in obtaining uniform films at atmospheric pressure, but good results, yielding highly conducting specular or textured films were obtained at low pressure and temperature (below 200°C). The low temperature films are a satisfactory alternative to ITO for the rear contact.

Conducting transparent zinc oxide films have been sputtered at room temperature from ZnO - Al_2O_3 targets using rf power. Devices prepared with ZnO/Ag yield equivalent performance to ITO/Ag. Work is continuing on reactively sputtering the conducting oxide from a low-cost metal target.

Measurements reveal that the reflectivity at the ITO/Ag interface is much lower than expected based on calculations. A promising solution for the problem has been developed whereby a transparent diffusion barrier placed between the ITO and Ag layers increases the reflectivity to nearly the values expected based on theory.

Module Research

Triple junction a-Si:H/a-Si:H/a-SiGe modules have been fabricated with a SERI-verified initial efficiency of 9.27%. The modules with an area over 900 cm^2 utilize a highly reflecting ITO/Ag rear contact with module patterning of all three levels (SnO_2, semiconductor and rear contact) being performed by laser patterning yielding an active to aperture area ratio of 98%. The design of the module, particularly the strip width, was selected based on a model to minimize power losses. A significant challenge to overcome is avoiding the shunting induced by laser recrystallization of the semiconductor. Based on model calculation this module is expected to degrade about 15% after 1000 hours of exposure at open circuit voltage.

The stability of the first modules with initial conversion efficiencies between 6.5% - 7.5% was evaluated by light-soaking the unencapsulated modules indoors at open circuit voltage. The modules had middle i-layer thickness between 4000Å-8000Å. The modules with thicker middle junction i-layer thickness degrade faster as expected. The best module, with a 4000Å middle junction i-layer degrades less than 10% after 1000 hours. All triple junction modules degrade at rates less than or equal to a 2000Å tandem a-Si:H/a-Si:H module.

TABLE OF CONTENTS

1.0 INTRODUCTION 1

2.0 SEMICONDUCTOR MATERIALS AND DEVICES 2
2.1 SiGe ALLOYS: Effect of H-Dilution on Structure 2
2.2 a-Ge:H by D.C. and RF Glow-Discharge 7
2.3 Thickness Dependence of Photoelectronic Properties 8
2.4 "AD HOC" Model of Triple Junction Multijunction Stability 15
2.5 Microcrystalline Si Formed by Rapid Thermal Anneal 23

3.0 NON-SEMICONDUCTOR MATERIALS RESEARCH 28
3.1 Atmospheric and Low Pressure CVD (LPCVD) of ZNO 28
3.2 Sputtered Zinc Oxide Films 39
3.3 Alternate Rear Reflectors 39

4.0 SUBMODULE RESEARCH 44
4.1 Introduction 44
4.2 Submodule Design 44
4.3 Progress Toward an 8.8% Stabilized Module 46
4.4 Defects and Uniformity of Modules 48
4.5 Optical Modeling of Triple Stacked Cells 53
4.6 Improvements in the Recombination Layer (Tunnel Junction) 57
4.7 Other Subtask Research Activities 57

REFERENCES 57

FIGURE CAPTIONS

		Page
Figure 2-1.	Infrared absorbance data for a-SiGe:H films prepared with (a) no H_2-dilution, (b) 5:1 H_2:SiH_4 + GeH_4 dilution and (c) 20:1 dilution.	3
Figure 2-2.	Ratio of SiH_2/SiH bonding of a-SiGe:H samples prepared without hydrogen dilution, with 5:1 dilution and with 20:1 dilution (H_2:(SiH_4 + GeH_4)) as a function of optical bandgap.	5
Figure 2-3.	Mobility lifetime product of a-SiGe:H samples prepared with 5:1 and 20:1 dilution (H_2:(SiH_4 + GeH_4)) as a function of optical bandgap.	6
Figure 2-4.	Thickness dependence of photocurrent (a) and ambipolar diffusion length (b) of a-Si:H measured with a He-Ne laser at ~ 60 mW/cm^2. Solid and dashed curves are calculated for surface recombination velocities of S=∞, 100, and 1 cm/s.	10
Figure 2-5.	Normalized efficiency of 2400Å i-layer a-SiGe:H devices deposited with and without hydrogen dilution.	16
Figure 2-6.	Normalized efficiency of a triple junction device with the configuration shown as a function of time, exposed at temperatures of 30°C, 40°C, 50°C and 60°C.	18
Figure 2-7.	Normalized 1000 hr. efficiency as a function of the optical bandgap of the bottom cell in a triple junction device. Calculations performed for a 50°C exposure temperature.	19

Page

Figure 2-8. Comparison of the predicted 1000 hr. performance of triple junction cells with experiment. The normalized efficiency is plotted as a function of the middle i-layer thickness. Shown for comparison is the expected 1000 hr. performance of single junction devices. 21

Figure 2-9. Calculated initial and 1000 hr. (1 year) stabilized performance of triple junction devices as a function of the middle junction i-layer thickness. 22

Figure 2-10. Arrhenius plot of the conductivity of thin (200Å) silicon films before and after crystallization by rapid thermal anneal (RTA). Both p-type and n-type films are shown. 24

Figure 2-11. Plot of the dependence of conductivity on film thickness. Typically, the conductivity decreases rapidly as thickness decreases below about 800Å for material which is plasma deposited under "microcrystalline growth" conditions. Exceptional behavior is exhibited for the films crystallized by RTA, as shown. 25

Figure 2-12. Optical transmission measurements of a p-type silicon film before and after crystallization via RTA. A noticeable decrease in the optical absorption coefficient, as expected for μ-xtal vs. amorphous material, is evidenced as greater optical transparency in the 400 to 600nm range. 26

Figure 3-1. Apparatus for the atmospheric deposition of zinc oxide from water and diethylzinc vapor. 30

Figure 3-2. Apparatus for the low pressure deposition of zinc oxide. 31

		Page
Figure 3-3.	Growth rate of zinc oxide films from diethylzinc and water by low pressure vapor deposition as a function of temperature.	32
Figure 3-4.	Resistance (ohm/sq) in zinc oxide films of similar thicknesses as a function of dopant (trimethylboron) flow.	34
Figure 3-5.	Dependence of zinc oxide film resistance on film thickness.	35
Figure 3-6.	Transmission and reflectance spectra of a specular (haze of 0.3%) film of zinc oxide.	36
Figure 3-7.	Transmission and reflectance spectra of a slightly textured (haze of 6.1%) film of zinc oxide.	37
Figure 3-8.	Transmission and reflectance spectra of a textured (haze of 17.9%) film of zinc oxide.	38
Figure 3-9.	Current - voltage curve of single junction solar cell with zinc oxide/silver rear contact.	40
Figure 3-10.	Quantum efficiency of single junction solar cell with zinc oxide/silver rear contact.	41
Figure 3-11.	Measured reflectivity (after correction for light-trapping effects) of a standard (ITO/Ag) textured reflector and an improved reflector under development at Solarex.	43
Figure 4-1.	The power output of a triple stack module and the major power losses as a function of the number of segments in the module.	45

Page

Figure 4-2. Indoor degradation data of triple junction modules (unencapsulated) as a function of time. Modules are referred to by the thickness of the middle junction or i_2 layer. Also shown for comparison is data for an a-Si:H/a-Si:H module with a bottom i-layer thickness of 2500Å. 47

Figure 4-3. Comparison of the indoor and outdoor stability measurements of encapsulated triple-stack modules. 49

Figure 4-4. The indoor degradation of modules having different i_2 layer thicknesses. 50

Figure 4-5. The variation in J_{sc} over a 12" x 13" module. 52

Figure 4-6. Expected quantum efficiency for the limiting case of no optical losses due to doped layers preceding the second intrinsic layer, complete collection is also assumed. 54

Figure 4-7. Quantum efficiency of an actual triple stack cell having a 6000Å I-2 layer. Due to improvement in doped layers, the QE currents collected in the intrinsic layers approach those predicted by the optical model for this type of cell. 56

LIST OF TABLES

		Page
Table 2-1	Some Properties of Representative a-Ge:H Films	8
Table 2-2	Initial and 1000 hr. (1 year) Stabilized Performance of a-Si:H (1.7 eV)/a-Si:H (1.7 eV)/a-SiGe:H (1.4 eV) Devices. V_{oc} is Taken as 0.55 Eg and the Initial Fill Factor is Assumed to be 0.7	20
Table 3-1	Electrical and Optical Properties of Typical ZnO Films Prepared by CVD	33
Table 4-1	The Variation in CTO Haze and Uniformity over a 12"x13" Substrate	51
Table 4-2	Projected J_{sc} of Triple Junction Cells as a Function of i-Layer Thickness Assuming No Improvement in Front Contact or Doped Layers	53
Table 4-3	Triple Cell Optical Absorption (In Terms of mA/cm^2)	55

1.0 INTRODUCTION

The present effort seeks to develop modules with a stabilized performance of 8.8% aperture area conversion efficiency after 600 hours light exposure (AM1.5) at 50°C in modules with aperature areas over 900 cm^2. Good progress towards this goal has been obtained with the demonstration of 9.3% initial performance in a submodule incorporating devices with relatively thin middle junction i-layer thickness of 6000Å. Devices with this design are expected to lose about 15% of their initial performance after 1000 hours of exposure.

Achieving long-term stabilized efficiencies of 12% or more requires substantial improvements in materials and devices. Our analysis has shown that substantial optical losses occur at both front and rear contacts which we hope to address with ZnO films prepared by CVD and sputtering processes now under development. Further progress in doped layers and alloys are also needed. Fundamental studies of the relationship between material structure and processes (particularly the effect of hydrogen dilution) are reported here.

2.0 SEMICONDUCTOR MATERIALS AND DEVICES

2.1 SiGe ALLOYS: EFFECT OF H-DILUTION ON STRUCTURE

In last year's annual report (2), we had shown that H_2-dilution (up to 5:1 H_2:(SiH_4 + GeH_4)) can significantly improve the transport properties of a-SiGe:H alloys. The ambipolar diffusion length, for instance, is increased by more than 15% using H_2-dilution. Raman scattering experiments, showed that H_2-dilution can substantially reduce bonding inhomogeneity in the alloy, which was found to be correlated to the photoelectronic properties of the material (3).

Here, we report further studies using IR spectroscopy to investigate the effect of H_2-dilution on the alloy microstructure revealed through H bonding configurations. Favorable changes in the H bonding structure of films made with H_2-dilution were observed. This has led us to further increase the amount of H_2-dilution used in the plasma deposition. As a result, a large increase in photoconductivity has been obtained in alloy films made with 20:1 H_2-dilution over a bandgap range between 1.45 eV and 1.65 eV. The effect of cell structure, e.g., the interface buffer layer, on the device performance has also been studied.

Figure 2-1 shows the IR transmission spectra of the Si-H and Ge-H stretch bands for three series of SiGe alloy films made with (a) no H_2-dilution, (b) 5:1 H_2-dilution, and (c) 20:1 H_2-dilution. The interference fringes in the spectra have been fitted and subtracted. The fraction of GeH_4 in the total of SiH_4 + GeH_4 is given for each spectrum in the figure, which is roughly proportional to the Ge content in the film and, to a large degree, determines the optical bandgap of the alloy. Four characteristic modes are commonly identified in the IR absorption band of SiGe alloys - the Si mono- and dihydride modes centered at ~ 2000 cm^{-1} and ~ 2075 cm^{-1}, respectively, and the similar pair for Ge centered at ~ 1880 cm^{-1} and ~ 1975 cm^{-1}, respectively.

Since Ge-H modes are much weaker than the Si-H ones in the IR spectra, due to preferential bonding of H to Si (4), and the Ge dihydride mode almost completely overlaps the Si mono-hydride mode, it is difficult to obtain detailed information on Ge-H bonding from the IR spectra. However, the effects of alloying Ge with Si and H_2-dilution on the Si-H modes are quite pronounced, as shown in **Figure 2-1**.

Figure 2-1. Infrared absorbance data for a-SiGe:H films prepared with (a) no H_2-dilution, (b) 5:1 H_2:SiH_4 + GeH_4 dilution and (c) 20:1 dilution.

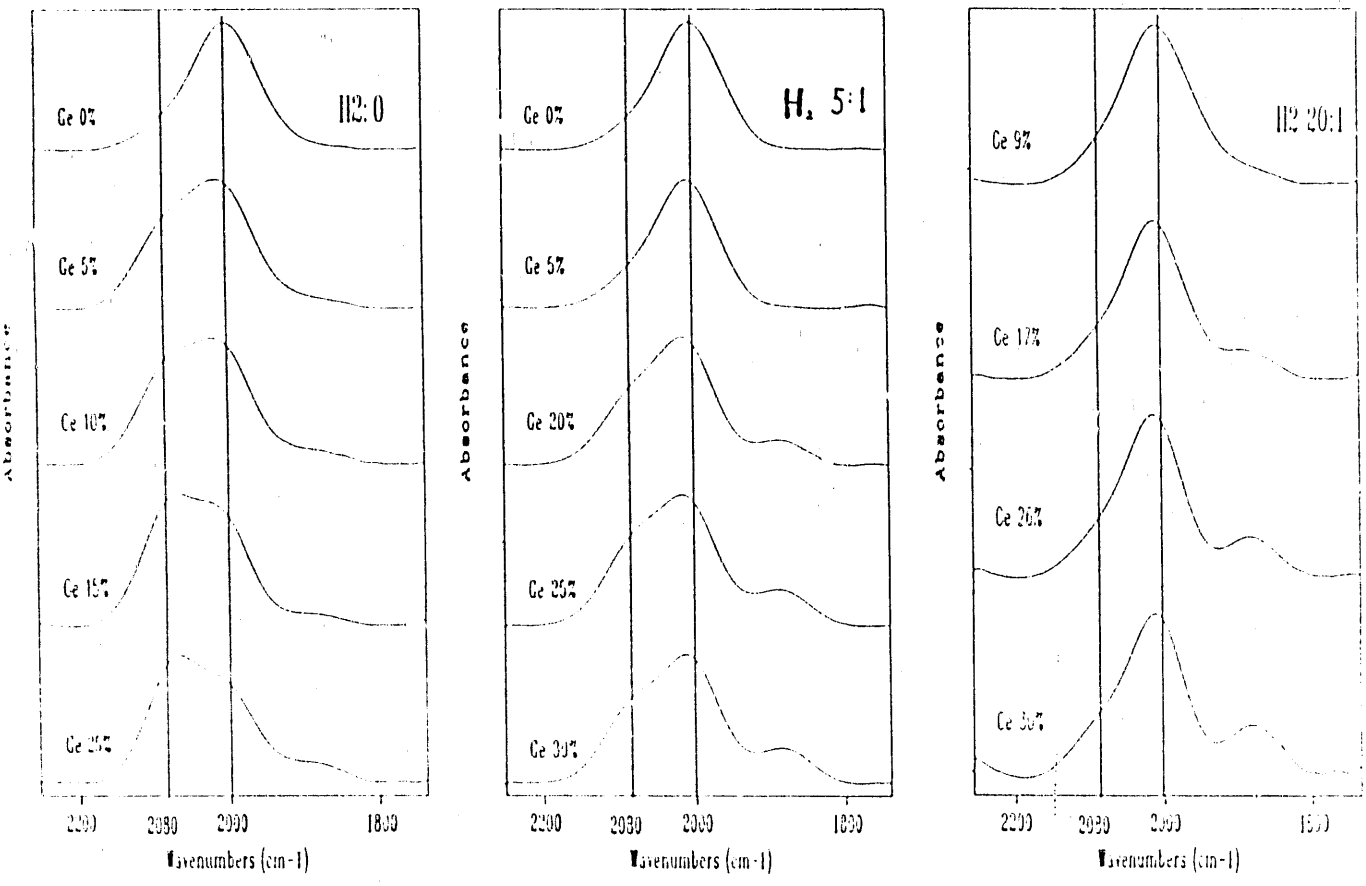

For films made with no H_2-dilution, **Figure 2-1**(a), the Si dihydride mode is greatly enhanced with increasing GeH_4 concentration. Some other researchers have also observed this phenomenon and have speculated that it is due to the low surface mobility of the Ge species which causes the formation of voids in the alloy material. While a similar effect is also present in the other two series, as shown in **Figure 2-1**(b) and (c), the magnitude of Si dihydride mode is dramatically suppressed by H_2-dilution. The possible explanations for this effect are that the growing surface can be covered by H much more effectively with H_2-dilution, which enhances the surface mobility of the Ge species, and that H_2-dilution can selectively etch away less densely bonded structures which presumably include the dihydride groups seen in the IR spectra. We have quantitatively modeled the IR spectra using three gaussians: two narrow peaks for the Si mono- and dihydride modes with FWHM of ~ 80 cm^{-1} and a broad one for the Ge hydrides with FWHM of ~110 cm^{-1} centered ~ 1900 cm^{-1}. **Figure 2-2** shows the ratio of the integrated intensities of Si mono- to dihydride components for the three series of alloy films. The effects described qualitatively above are clearly exhibited.

While the effect of suppressing IR Si dihydride mode becomes less pronounced with H_2-dilution from a dilution ratio of 5:1 to 20:1, as shown in **Figure 2-2**, a large increase in the steady state photoconductivity has been observed in the bandgap range between 1.45 eV and 1.6 eV for samples made with 20:1 H_2-dilution. **Figure 2-3** shows the $\mu\tau$ product of the alloy films made with various H_2-dilution. It is quite remarkable that the $\mu\tau$ product at a bandgap ~ 1.55 eV can be in the 10^{-6} cm^2/V range using 20:1 H_2-dilution, which is even larger than that for good a-Si:H. The ambipolar diffusion lengths of these films are about the same as for the samples made with 5:1 H_2-dilution.

We have done some preliminary studies to test alloy materials made with 20:1 H_2-dilution in a device configuration. It was found that the structure of the device plays an important role in the device performance. For example, the standard device structure, which works very well for SiGe i-layers deposited with up to 5:1 H_2-dilution produces extremely poor devices when 20:1 H_2-dilution is used in the i-layer. Adding an ultra-thin buffer layer (~50Å thick) at the p/i interface can dramatically improve the fill factor of the solar cell. So far, such single junction SiGe cells have been made as good as (or slightly better than) those made with 5:1 H_2-dilution at the bandgap of ~ 1.46 eV. Optimization of the cell structure using 20:1 H_2-dilution is continuing.

Figure 2-2. Ratio of SiH_2/SiH bonding of a-SiGe:H samples prepared without hydrogen dilution, with 5:1 dilution and with 20:1 dilution (H_2:(SiH_4 + GeH_4)) as a function of optical bandgap.

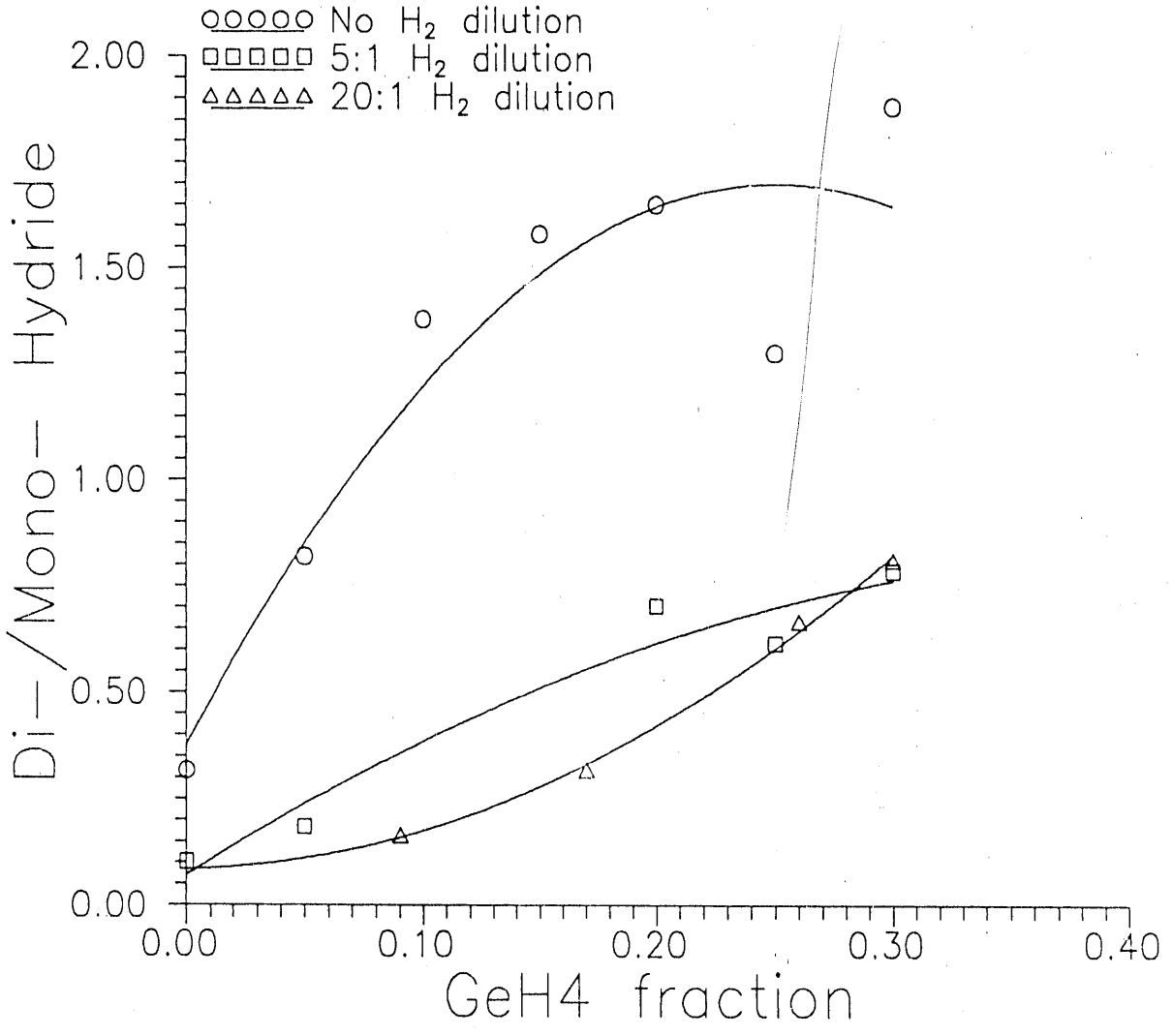

Figure 2-3. Mobility lifetime product of a-SiGe:H samples prepared with 5:1 and 20:1 dilution (H_2:(SiH_4 + GeH_4)) as a function of optical bandgap.

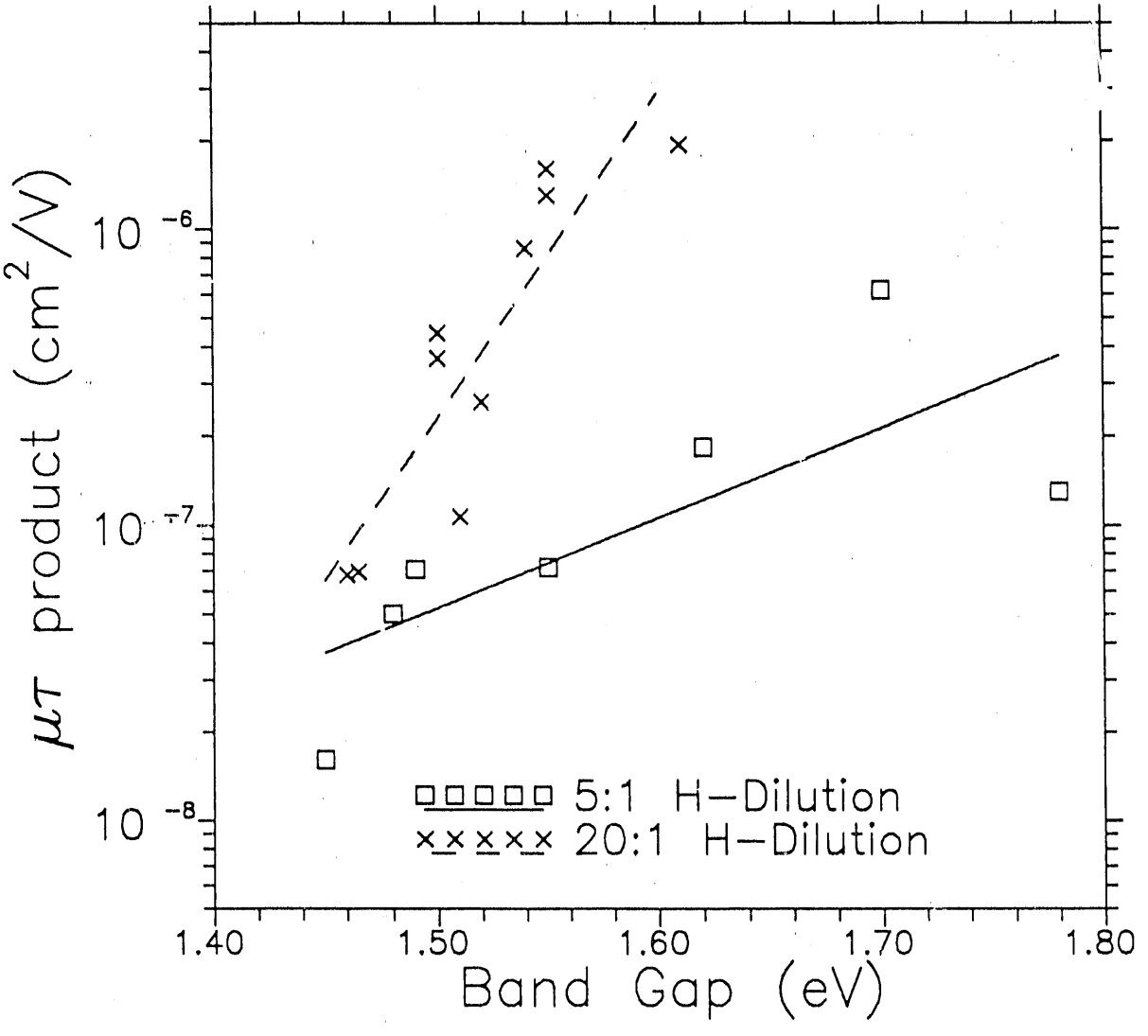

2.2 a-Ge:H BY D.C. AND RF GLOW-DISCHARGE

In order to evaluate the potential of undoped a-Ge:H for use in multijunction solar cells, and to gain insights into the preparation of high quality a-$Si_{1-x}Ge_x$:H of high x, two series of a-Ge:H films were produced by rf and dc glow-discharge method, respectively, using GeH_4 and H_2 under a variety of conditions so as to optimize the properties of a-Ge:H.

Attempts were made to reproduce the high-quality, rf glow-discharge produced a-Ge:H films recently reported by the Harvard group (1) by placing substrates on the powered electrode (as well as on the unpowered electrode). The resulting films are quite photoconductive (see **Table 2-1**) and contain a significant amount (~15% to 20%) of hydrogen. Since the dark conductivity σ_{dark} is also high, the high $n\mu\tau$ is likely to be caused by the proximity of the Fermi-level to the transport level, as suggested by the values of the activation energy E_σ for σ_{dark}. In contrast to the Harvard result, the films from the powered electrode are only somewhat better than those from the unpowered electrode as measured by $n\mu\tau$, the ratio of $n\mu\tau$ to σ_{dark}, and the apparent ambipolar diffusion length L (measured at 1.96 eV and taken as a lower-bound estimate). The best L obtained is smaller than the Harvard film (380 vs. 600Å). Infrared measurements reveal no evidence of atmospheric contamination. In brief, without systematically varying all the controllable parameters, we have not been able to duplicate the Harvard films under nominally identical (or otherwise) conditions. It appears that the deposition hardware (the layout of the reactor) may play an important role in determining film growth process.

Cathodic d.c. glow-discharge produced a-Ge:H were fabricated with different H_2-dilution ratios, d.c. current, and temperature. Films were made both by placing substrates on the normal cathode *and* by placing substrates on the normal anode but with reversed polarity of the d.c. power supply (the two methods produced similar films). Also produced were a number of conventional (anodic) d.c. films for comparison. The transport properties of the cathodic films show improvements over those of the (usual) anodic films. This fact is not inconsistent with the notion that ion bombardment, which occurs at the cathode, can be beneficial for the growth of good a-Ge:H by forcing structural rearrangements. Unlike rf and anodic d.c. glow-discharge produced films, the H_2-dilution ratio had no strong effect on the measured properties of the cathodic samples. A serious limitation of cathodic d.c. technique is the (very) low growth rate and the film non-uniformity. This is attributable to the insulating substrates which are poor choices for the cathode in a d.c. discharge environment.

Table 2-1
Some Properties of Representative a-Ge:H Films

	Growth Rate (Å/sec)	Bandgap (eV)	σ_{dark} (S/cm)	act. energy E_σ (eV)	$\eta\mu\tau$ (cm^2V^{-1})	Diffusion Length (Å)
dc anodic	2.5	1.0	$2x10^{-4}$	0.38	$3x10^{-7}$	about 300
dc cathode	0.8-0.1	1.0	$1x10^{-4}$	0.34	$1x10^{-7}$	460
rf PECVD	1.5	n/a	$8x10^{-5}$	0.36	$2x10^{-7}$	380
Harvard	near 4	1.1(1)	$2x10^{-6}$	0.49	$3x10^{-7}$	600

2.3 THICKNESS DEPENDENCE OF PHOTOELECTRONIC PROPERTIES

The photoelectronic properties of amorphous hydrogenated silicon (a-Si:H) film are known to be influenced by the surface or near surface layer (5). However, because these surface effects are not very well understood, they are often ignored in the interpretation of experimental results. The main experimental difficulty is that there are no techniques which can directly probe the photoelectronic properties of the surface. Although surfaces are often investigated by studying the thickness or wavelength dependence of material properties, detailed mathematical analysis is generally not feasible to quantify the surface effects due to the lack of a few key parameters. One particular example is the ambipolar diffusion length which is a crucial parameter in determining the effect of surface/interface recombination, but had not been reliably measured until very recently. Therefore, the development of the steady state photocarrier grating (SSPG) technique (6) which allows accurate determination of the ambipolar diffusion length in amorphous semiconductors offered a new opportunity for understanding certain surface recombination related effects. We have studied the thickness dependence of steady state photoconductivity and ambipolar diffusion length in a-Si:H. It is shown that both photoelectronic properties are strongly dependent on film thickness and the dependence can be mainly attributed to the effect of surface recombination. A lower limit on the surface/interface recombination velocity is determined from the quantitative analysis. Other related experimental observations, such as wavelength dependence of diffusion length and photoconductivity, are also discussed and are shown to be consistent with this interpretation.

The a-Si:H films of thickness between 0.1 μm and 2.0 μm were deposited by d.c. glow discharge of pure silane on fused silica substrates. The deposition conditions were the same as used to make i-layers in high efficiency a-Si:H solar cells. Coplanar nichrome electrodes, predeposited on the substrates, were used for the electrical measurements. Ambipolar diffusion length was measured using the SSPG technique with either a He-Ne laser at $\lambda = 632.8$nm or an Ar laser at $\lambda = 514.5$nm. The light intensity used was approximately 60 mW/cm^2 in all cases. The angle between the two laser beams was varied between 10° and 45°. The thickness dependence of d.c. photocurrent was also measured using the same experimental setup with laser light illumination. The wavelength dependence of the photocurrent, on the other hand, was measured using interference filters under white light illumination. The measured photocurrent was normalized by the photon flux detected by a calibrated photodiode.

Figure 2-4 (a) and (b) show the thickness dependence of photocurrent (I_p) in open circles and ambipolar diffusion length (L) in open squares measured with illumination from the He-Ne laser. As has been shown, steady state photoconductivity and ambipolar diffusion length characterize transport properties of photoexcited electrons and holes, respectively, in the material (6,7). The large decrease in both measured properties with decreasing thickness, therefore, suggests that the photoelectronic properties in the region near the free surface and the film/substrate interface are much poorer than in the bulk. While this may result from a severe structural inhomogeneity or other complex phenonema, we first consider the effect of surface/interface recombination which is very likely to be present.

Under the assumption that carrier lifetime τ does not change with concentration, the density of photogenerated carriers in the presence of surface/interface recombination is governed by the diffusion equation,

$$D \frac{d^2N(z)}{dz^2} - \frac{N(z)}{\tau} + G_0 e^{-\alpha z} = 0 \qquad (1)$$

and the boundary conditions at the surface (z = 0) and the film/substrate interface (z = d),

Figure 2-4. Thickness dependence of photocurrent (a) and ambipolar diffusion length (b) of a-Si:H measured with a He-Ne laser at ~ 60 mW/cm^2. Solid and dashed curves are calculated for surface recombination velocities of S=∞, 100, and 1 cm/s.

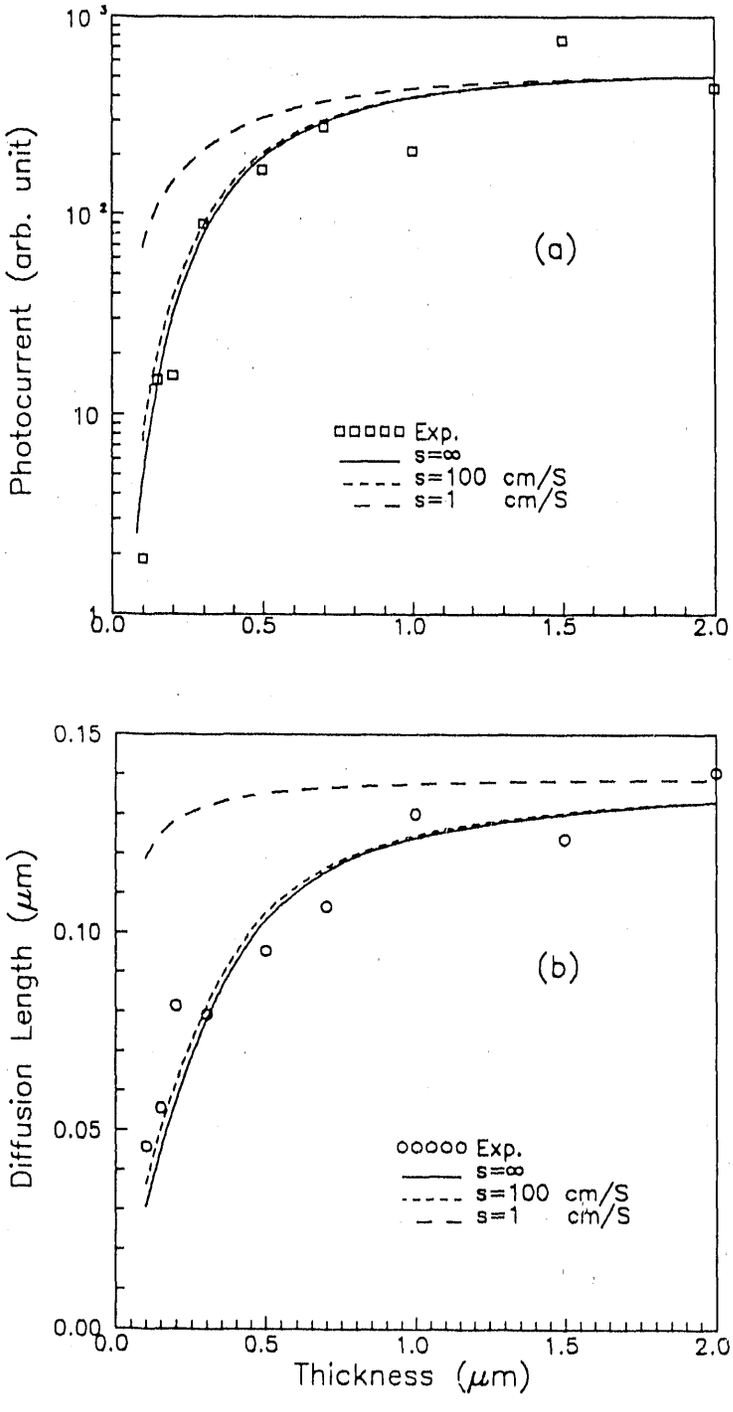

$$D\frac{dN}{dz}\Bigg|_{z=0} = S_1 N(0) \text{ and } -D\frac{dn}{dz}\Bigg|_{z=d} = S_2 N(d) \qquad (2)$$

where D is the ambipolar diffusion coefficient, τ the lifetime and $G_0 e^{-\alpha z}$ is the carrier generation term in which α is the optical absorption coefficient. S_1 and S_2 are the recombination velocities at the respective surface/interface. Since measurements with illumination from either side of the film show little difference, we assume $S_1 = S_2 = S$ for simplicity.

The resulting carrier density distribution N(z) consists of three exponential terms corresponding to the original exponential carrier generation and the recombination at both the surface and the film/substrate interface,

$$N(z) = \frac{G_0\tau}{1-(L_0\alpha)^2}\left[e^{-\alpha z} + A(L_0)e^{-z/L_0} + B(L_0)e^{z/L_0} \right] \qquad (3)$$

where $L_0 = \sqrt{D\tau}$ is the ambipolar diffusion length. The coefficients $A(L_0)$ and $B(L_0)$ are expressed in the following form where $\mathfrak{L}$ is simply a dummy variable,

$$A(\mathfrak{L}) = \frac{1-S\mathfrak{L}/D)(\alpha\mathfrak{L}-S\mathfrak{L}/D)e^{-\alpha d} - (1+S\mathfrak{L}/D)(\alpha\mathfrak{L}+S\mathfrak{L}/D)e^{d/\mathfrak{L}}}{1+S\mathfrak{L}/D)^2 e^{d/\mathfrak{L}} - (1-S\mathfrak{L}/D)^2 e^{d/\mathfrak{L}}} \qquad (4a)$$

$$B(\mathfrak{L}) = \frac{1+S\mathfrak{L}/D)(\alpha\mathfrak{L}-S\mathfrak{L}/D)e^{-\alpha d} - (1-S\mathfrak{L}/D)(\alpha\mathfrak{L}+S\mathfrak{L}/D)e^{-d/\mathfrak{L}}}{1+S\mathfrak{L}/D)^2 e^{d/\mathfrak{L}} - (1-S\mathfrak{L}/D)^2 e^{-d/\mathfrak{L}}} \qquad (4b)$$

Since the photocurrent is proportional to the integral of N(z) over the film thickness, then

$$I_p \sim \frac{G_0 \tau L_0}{1-(L_0\alpha)^2}\left[\frac{1}{L_0\alpha}(1-e^{-\alpha d}) + A(L_0)\ (1-e^{-d/L_0}) + B(L_0)\ (e^{d/L_0}-1)\right] \qquad (5)$$

On the other hand, the ambipolar diffusion length is derived in SSPG experiments from the ratio of photoconductance under the illumination of an interference grating to that under uniform illumination (5). Therefore, we must also solve the diffusion equation with a sinusoidal carrier generation term along the x-axis in parallel with the film surface, corresponding to the shallow interference grating in SSPG. The 2-dimensional diffusion equation describing the carrier distribution due to the small modulation is,

$$D\left[\frac{\partial^2 \Delta N(x,z)}{\partial z^2} + \frac{\partial^2 \Delta N(x,z)}{\partial z^2}\right] - \frac{\Delta N(x,z)}{\tau} + \Delta G e^{-\alpha z} \cos\left[\frac{2\pi x}{\Lambda}\right] = 0 \qquad (6)$$

where Λ is the grating period. The boundary conditions for ΔN at $z = 0$ and $z = d$ are the same as in Equation (2). The solution for Equation (6) is,

$$\Delta N(x,z) = \frac{\Delta G \tau \cos(\pi x/\Lambda)}{1+(2\pi L_0/\Lambda)^2-(L_0\alpha)^2}\left[e^{-\alpha z} + A(L')e^{-z/L'} + B(L')e^{z/L'}\right] \qquad (7)$$

$$L' = \sqrt{\frac{L_0^2}{1+(2\pi L_0/\Lambda)^2}}$$

where and coefficients A(L') and B(L') can be calculated using Equations (4a) and (4b) with L' as the diffusion length parameter replacing the dummy variable $\mathfrak{L}$. It is interesting to note that the lateral sinusoidal modulation alters the crucial diffusion length parameter. In fact, it is the Λ-dependent alteration that causes the large thickness dependence in the measured diffusion length, as will become clear below. Following the theory of SSPG (5), the measured photoconductance ratio, β, can be calculated using Equations (4) and (7), i.e.,

$$\beta = 1-2\phi \left[\frac{1-(L_0\alpha)^2}{1+(2\pi L_0/\Lambda)^2-(L_0\alpha)^2}\right] \frac{2\int_0^d f^2(z,l')/f(z,L_0)\,dz}{\int_0^d f(z,L_0)\,dz} \qquad (8)$$

where ϕ is a constant related to the exponent in the power law relationship between photoconductivity and the carrier generation rate, and

$$f(z,\mathfrak{L}) = e^{-\alpha z} + A(\mathfrak{L})e^{-z/\mathfrak{L}} + B(\mathfrak{L})e^{z/\mathfrak{L}} \qquad (9)$$

According to the experimental procedure (8), we first plot Λ^{-2} against $\sqrt{2/1-\beta}$ calculated from Equation (8) and then extrapolate the best linear fit of the plot to the vertical axis. The actual diffusion length L is then calculated from the intercept Λ_0^{-2} using the relationship $(1/2\pi L)^2 = \Lambda_0^{-2}$. In the experimentally used range of Λ^{-2}, a nearly perfect linear relationship between the two variables is obtained for all thicknesses from 0.1μm to 2.0μm. We note that in Eq. (8), the effect of surface recombination comes mainly from the difference between the two integrals. Since L' is smaller than L_0 and is Λ-dependent, the ratio of the two integrals is larger than unity and increases with decreasing Λ. Therefore, the measured diffusion length in the presence of surface recombination is smaller than the bulk value L_0.

The expected thickness dependence from Eqs. (4)-(9) for both photocurrent and diffusion length under the presence of surface/interface recombination are plotted as solid and dashed curves in **Figures 2-4** (**a**) and (**b**). Calculations for three characteristic surface recombination velocities, i.e. S=1, 100 and ∞ (cm/sec), are presented. The photocurrent is normalized to 500 on the relative scale at 2μm. The intrinsic diffusion length L_0 used in the calculations is 0.14μm which is essentially known from the saturation value of the measured diffusion lengths are large thicknesses. The other parameters used in the calculations are $D = 1\times10^{-4}$ cm^2/sec, estimated by assuming τ - 2×10^{-6} sec (9), and $\alpha = 1\times10^4$ cm^{-1}, the measured absorption coefficient. As shown in **Figure 2-4**, excellent fit to both sets of experimental data can be obtained for essentially any S value above 100 cm/sec. The reason that the thickness dependence is insensitive to S beyond a certain value is simply because the surface recombination is controlled by both the surface recombination velocity and the bulk diffusion coefficient. When S is higher

than a certain value, the recombination is strongly limited by the bulk diffusion. Since the actual S value is likely to be larger than 100 cm/s, at least for crystalline semiconductors (10), the thickness dependence can thus be mainly attributed to the effect of surface recombination.

We have also measured normalized photoconductance as a function of wavelength in the range 450 - 750nm and ambipolar diffusion length using an Ar laser at λ = 514.5nm. The major features in the wavelength dependence of normalized photoconductance agree well, in general, with the predicted effect of surface recombination. For instance, the photoconductance of thick samples show a decrease from the peak value at ~ 650nm to a value approximately an order of magnitude lower at 450nm. However, it is not straightforward to derive new information from such measurements. On the other hand, the diffusion length measurements at 514.5nm yielded values close to those measured at 632.8nm, despite a factor of 7 difference in the absorption length between the two wavelengths. While it seems surprising because the effect of surface recombination is obviously larger at shorter wavelengths, the observation in fact can be explained by the very same effect. Since the absorption length at 514.5nm ($\alpha^{-1} \simeq 0.07/\mu m$) is shorter than the diffusion length, the average carrier density in the film is greatly reduced by surface recombination to at least an order of magnitude lower than that at 632.8nm. Although surface recombination would tend to decrease the measured diffusion length, the much lower average carrier density, on the other hand, increases the carrier lifetime and thus compensates the loss.

As we mentioned earlier, the thickness dependence can, in principle, arise from certain structural inhomogeneity related to the growth process. However, the length scale of at least several thousand angstroms in the thickness dependence is apparently too large for most relaxation processes such as nucleation (11). We have done a number of experiments to examine whether impurities or annealing at the deposition temperature could be the cause. The results were, nonetheless, all negative. SIMS analysis, for example, indicated that impurity concentrations are very low throughout the films. The measurements on samples which were annealed in an H_2 atmosphere after deposition also showed little difference from those without such treatment. To address the question whether the material may improve during deposition, we have done measurements on samples whose thickness was reduced by plasma etching. Unfortunately, the poor control over the etching process resulted in non-reproducible properties, which may actually reflect the fact that the photoelectronic properties are strongly affected by the surface conditions.

We have shown that to a large extent the strong thickness dependence of the photoelectronic properties of a-Si:H can be attributed to the effect of surface or interface recombination. For the

typical untreated a-Si:H surface, the surface recombination velocity is likely to be larger than 100 cm/s. The bulk properties of the material can be directly obtained only from thick samples (≥1μm) and by using weakly absorbed light.

2.4 "AD HOC" MODEL OF TRIPLE JUNCTION MULTIJUNCTION STABILITY

Although it is clear that multijunction devices are more stable than their single junction counterparts, a quantitative relationship between device design parameters and the rate of light-induced change is lacking. For single junction devices we have observed that the performance of devices declines linearly with the logarithm of time at a rate which is determined by the i-layer thickness and temperature according to the relationship (12),

$$\eta(t)/\eta(0) = 1.1 - (1.28.10^{-6})\ d^{0.54}\ \exp(0.19/kT)\ \log(t/t_o) \qquad (10)$$

where (t,0) refer to the efficiency at time t and t = 0, d is the sample i-layer thickness in Angstroms and T is temperature. More recently, we have found that the rate constant for the degradation of a-SiGe:H alloys declines linearly with optical bandgap and is generally lower than than found for a-Si:H alloys, provided hydrogen dilution is used in preparation as shown in Figure 2-5. Bennett and Rajan (13) have shown that for silicon tandem cells that the overall rate of decline in the performance of devices upon light exposure was simply the arithmetic average of the individual cells. Assuming this relationship holds for triple junction cells, and that the i-layer thickness and temperature dependence remains constant allows us to write a more generalized expression for a triple junction device, namely,

$$\eta(t)\ /\ \eta(0) = \frac{1}{3}\sum_{i=1}^{3}\ [1.1\ -\ (K_i\ (d)^{0.54}\ \exp\ (0.19/kT))\ \log\ t/t_o] \qquad (11)$$

where K_i is the rate constant of the ith cell and the other symbols retain their previous meaning. Hence, we may predict the future performance of a triple junction cell based on its most important design parameters, i-layer thickness and optical bandgap, as well as the temperature at which the cell is degraded.

Figure 2-5. Normalized efficiency of 2400Å i-layer a-SiGe:H devices deposited with and without hydrogen dilution.

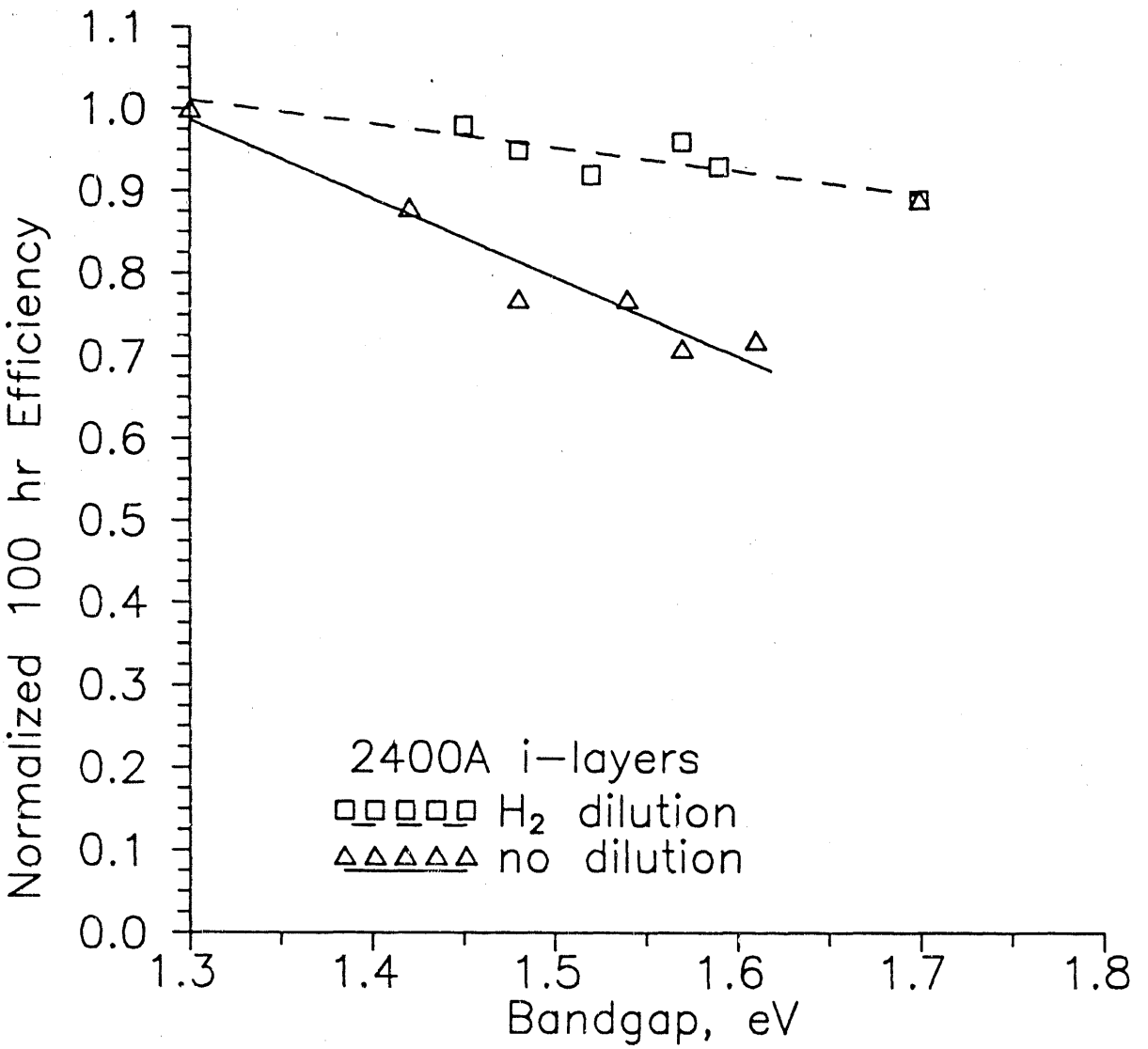

We now examine the implications of this model on the long-term performance of triple junction devices of various designs. **Figure 2-6** plots the time dependent normalized efficiency of a triple junction device for exposure temperatures between 30°C and 60°C. After 1000 hours of exposure, the performance varies from 82% of $\eta(t=0)$ at 30°C to 94% at 60°C. The very low degradation anticipated at 60°C exposure reflects the substantial effects of annealing experienced at the higher temperature. The impact of device design is shown in **Figure 2-6** for triple junction devices with optical bandgaps of 1.7 eV/1.7 eV/1.45 eV for i_1, i_2 and i_3, respectively, after 1000 hours exposure at various temperatures, and for an i_2 layer thickness between 4000Å and 8000Å. The thickness of i_1 and i_3 layers are adjusted to maintain current matching. Since the middle junction contains by far the thickest i-layer in the device, its degradation dominates the long-term performance. The comparatively thin i_1 and i_3 layers lower the overall rate of degradation since they are relatively little influenced by light exposure. For operation at 50°C, we find the overall 1000 hour performance decreases from 91% of $\eta(0)$ for a 4000Å thick (i_2) device to 86% for an 8000Å (i_2) triple junction cell.

As we have shown earlier, the rate of decline in performance upon light exposure of an a-SiGe:H solar cell decreases with optical bandgap. Hence, we expect a benefit in long-term performance for devices with lower bandgaps. The stability of the triple junction device is further enhanced by using low bandgap alloys, because thinner layers are required for current matching, further reducing the degradation rate. The model allows us to quantitatively verify this assumption. **Figure 2-7** plots the normalized efficiency as a function of the optical bandgap of the bottom junction device (i_3) for a cell in which the middle junction is 6000Å thick. As expected, the degradation is slightly larger for the higher bandgap cell, but over the range from 1.4 to 1.55 eV, the increase is only about 2%. It is unlikely that the small decrease in the rate of degradation would offset the higher performance obtained with the larger bandgap a-SiGe:H alloys. Even though theory predicts higher performance for devices with the lower i_3 bandgap, (1.45 eV being optimum) in practice, the poorer transport properties obtained with low bandgap alloys dominate the long-term efficiency.

It is worthwhile to compare the results of the ad hoc model with the results of experiments. A series of four triple junction devices with i_2 layers 2000Å, 4000Å, 6000Å and 8000Å thick were exposed to simulated AM1.5 illumination for 1000 hrs., i.e., the approximate equivalent of one year outdoors. The performance of two such sets of devices is compared with predictions of the

Figure 2-6. Normalized efficiency of a triple junction device with the configuration shown as a function of time, exposed at temperatures of 30°C, 40°C, 50°C and 60°C.

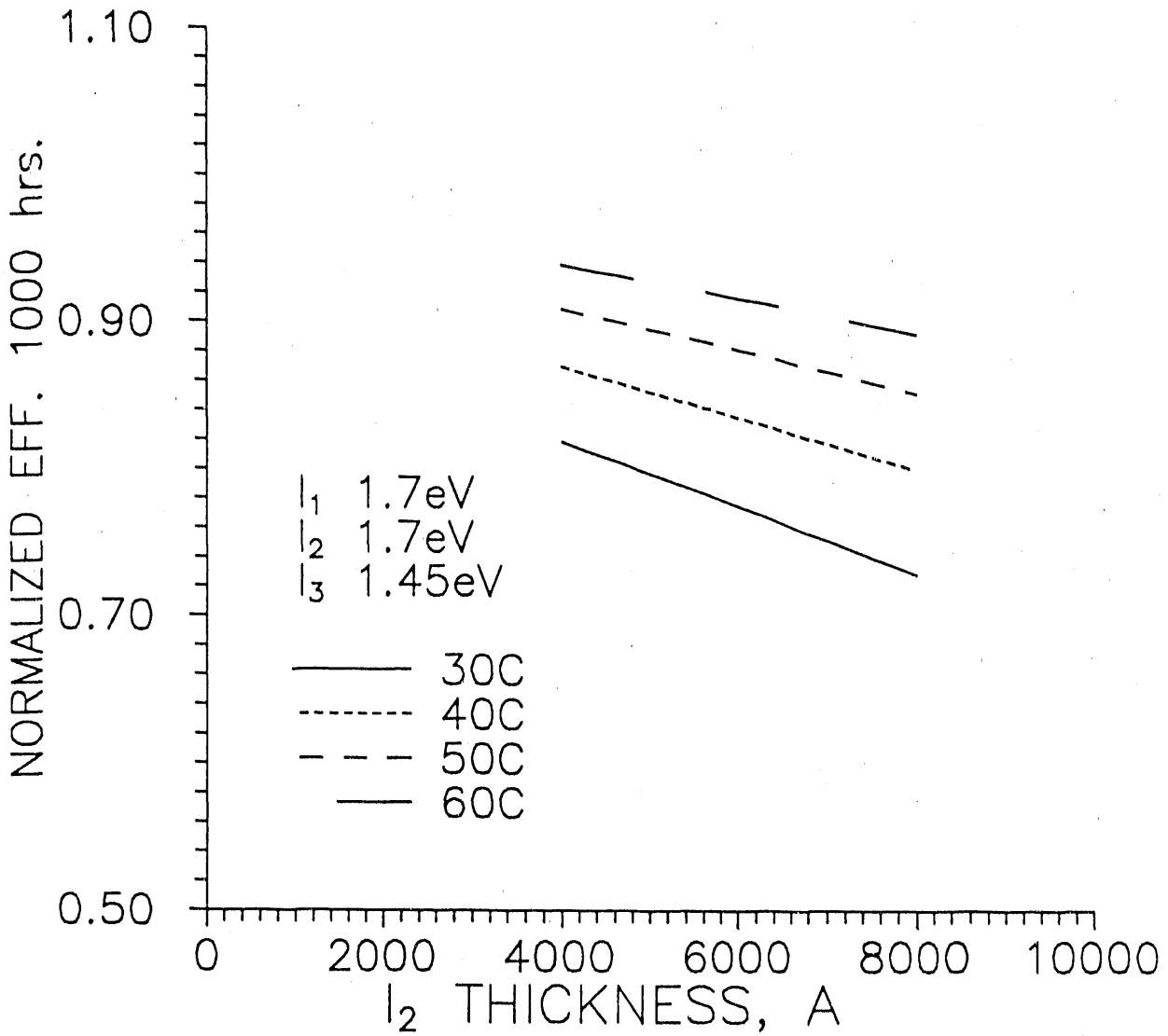

Figure 2-7. Normalized 1000 hr. efficiency as a function of the optical bandgap of the bottom cell in a triple junction device. Calculations performed for a 50°C exposure temperature.

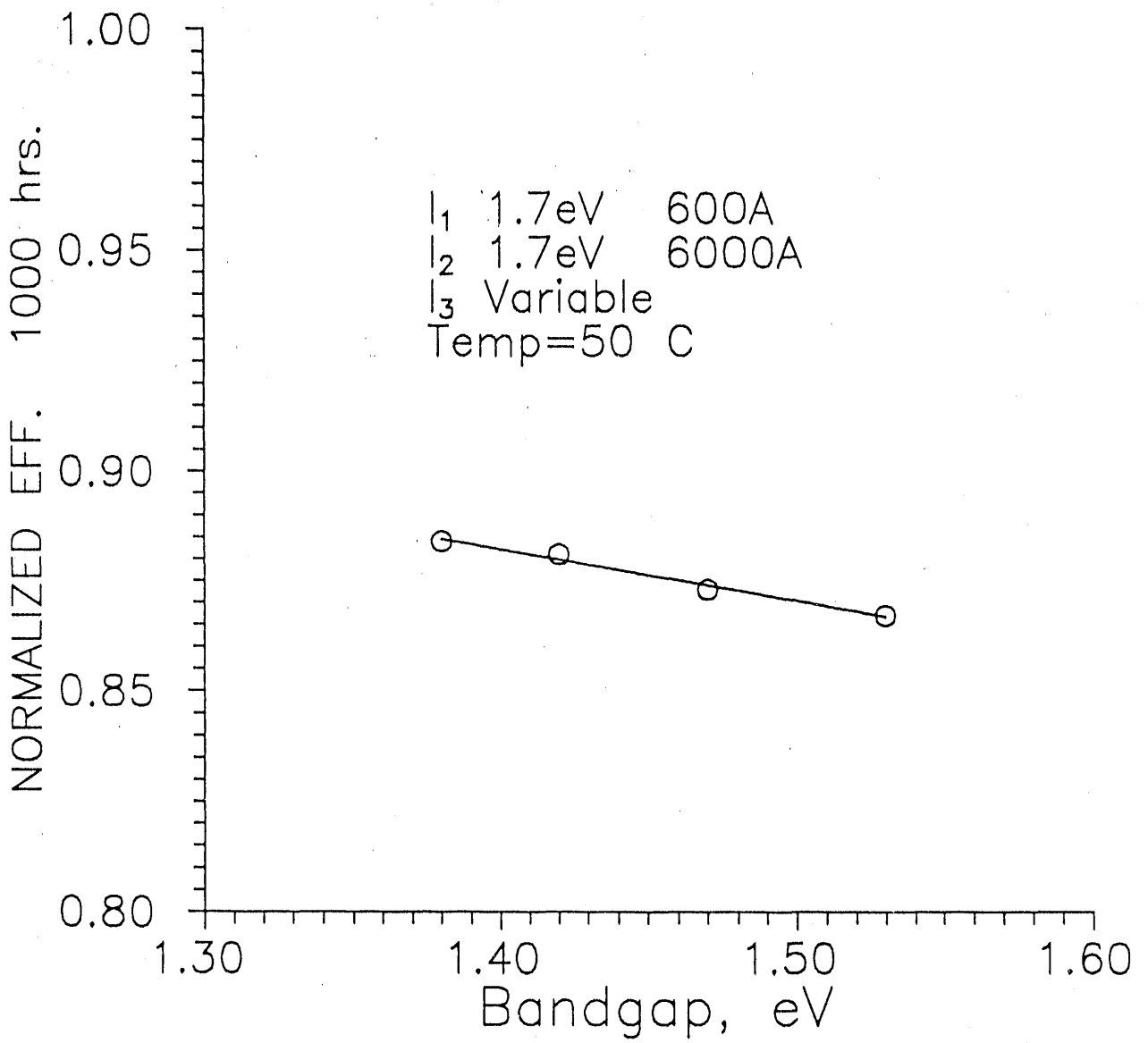

model in **Figure 2-8**. Very good agreement is found. It is especially noteworthy that the initial conversion efficiencies of some devices in this population is 9.6% and these cells retain 90% of this performance after 1000 hrs. of exposure. Also shown for comparison are the results expected for the degradation of single junction devices. The superior stability of the triple junction devices compared to the single junctions is clearly evident. While 0.8 μm thick single junction devices are expected to lose about 50% of their performance after 1000 hrs., the comparable 0.8 μm thick (middle junction) triple is expected to retain 82% of its initial efficiency.

We can calculate the stabilized efficiencies that triple junction devices should attain given modest improvements in material quality and device design. **Table 2-2** and **Figure 2-9** summarize the findings for several a-Si:H/a-Si:H/a-SiGe:H triple junction devices designed with the constraint that the middle junction i-layer remain the thickest undoped region in the device.

Table 2-2

Initial and 1000 hr. (1 year) Stabilized Performance of a-Si:H (1.7 eV)/a-Si:H (1.7 eV)/a-SiGe:H (1.4 eV) Devices. V_{oc} is Taken as 0.55 Eg and the Initial Fill Factor is Assumed to be 0.7

Junction Thickness, Å			J_{sc}	η/η_o	η_o	$\eta(1000)$
i_1	i_2	i_3				
400	8000	3000	7.85	.82	14.4%	11.8%
350	6000	2000	7.5	.86	13.76%	11.9%
300	4000	1500	7.23	.899	13.25%	12.01%
250	2000	750	6.41	.956	11.75%	11.2%

A relatively easily attainable value of 0.7 has been assumed for the initial fill factor. The initial conversion efficiency increases with thickness due to the higher short circuit current density; the thicker devices, however, have a higher rate of degradation. Thus, a very broad maximum of 12% in the stabilized efficiency occurs for devices with a middle junction i-layer of about 4000Å.

Figure 2-8. Comparison of the predicted 1000 hr. performance of triple junction cells with experiment. The normalized efficiency is plotted as a function of the middle i-layer thickness. Shown for comparison is the expected 1000 hr. performance of single junction devices.

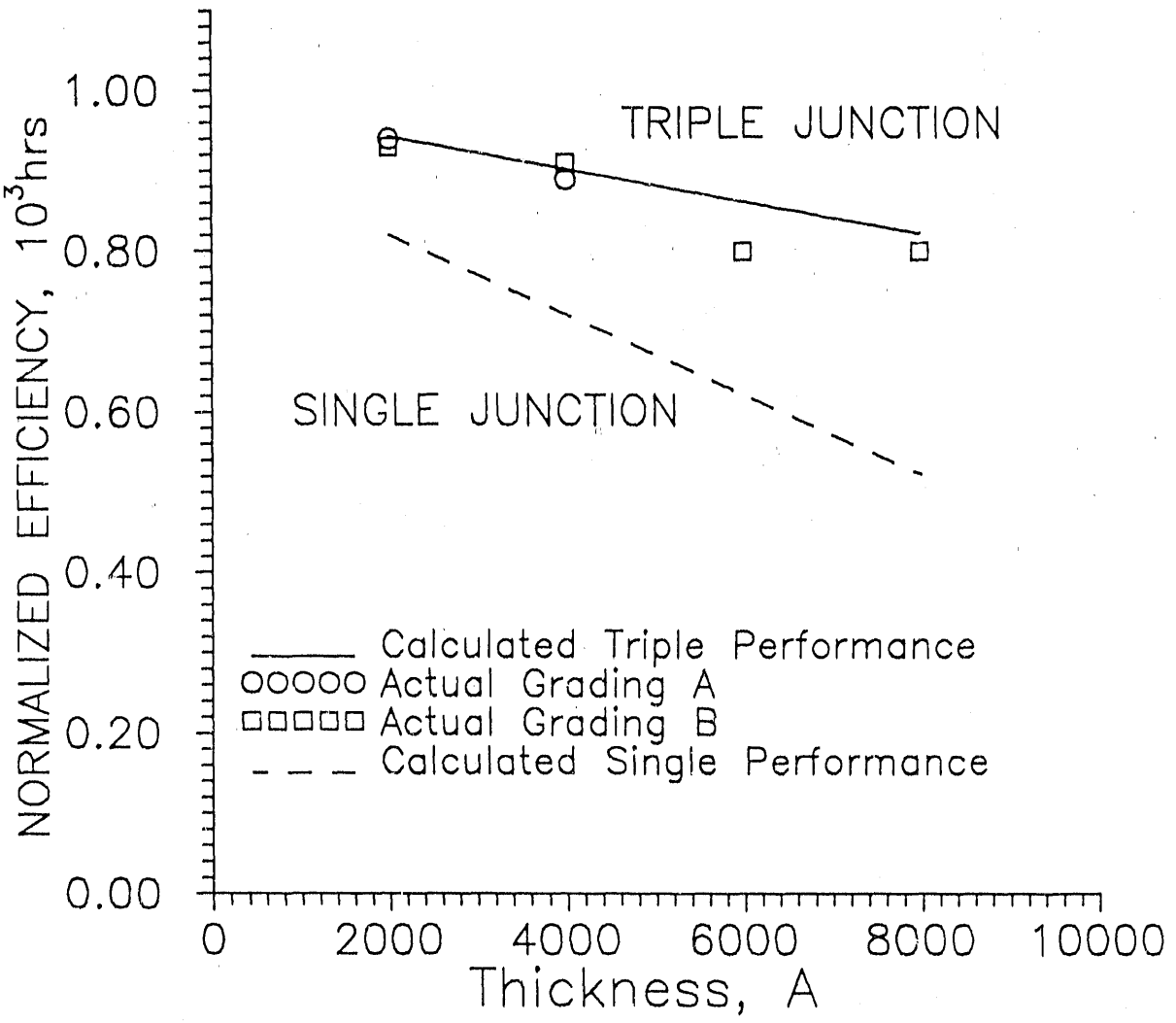

Figure 2-9. Calculated initial and 1000 hr. (1 year) stabilized performance of triple junction devices as a function of the middle junction i-layer thickness.

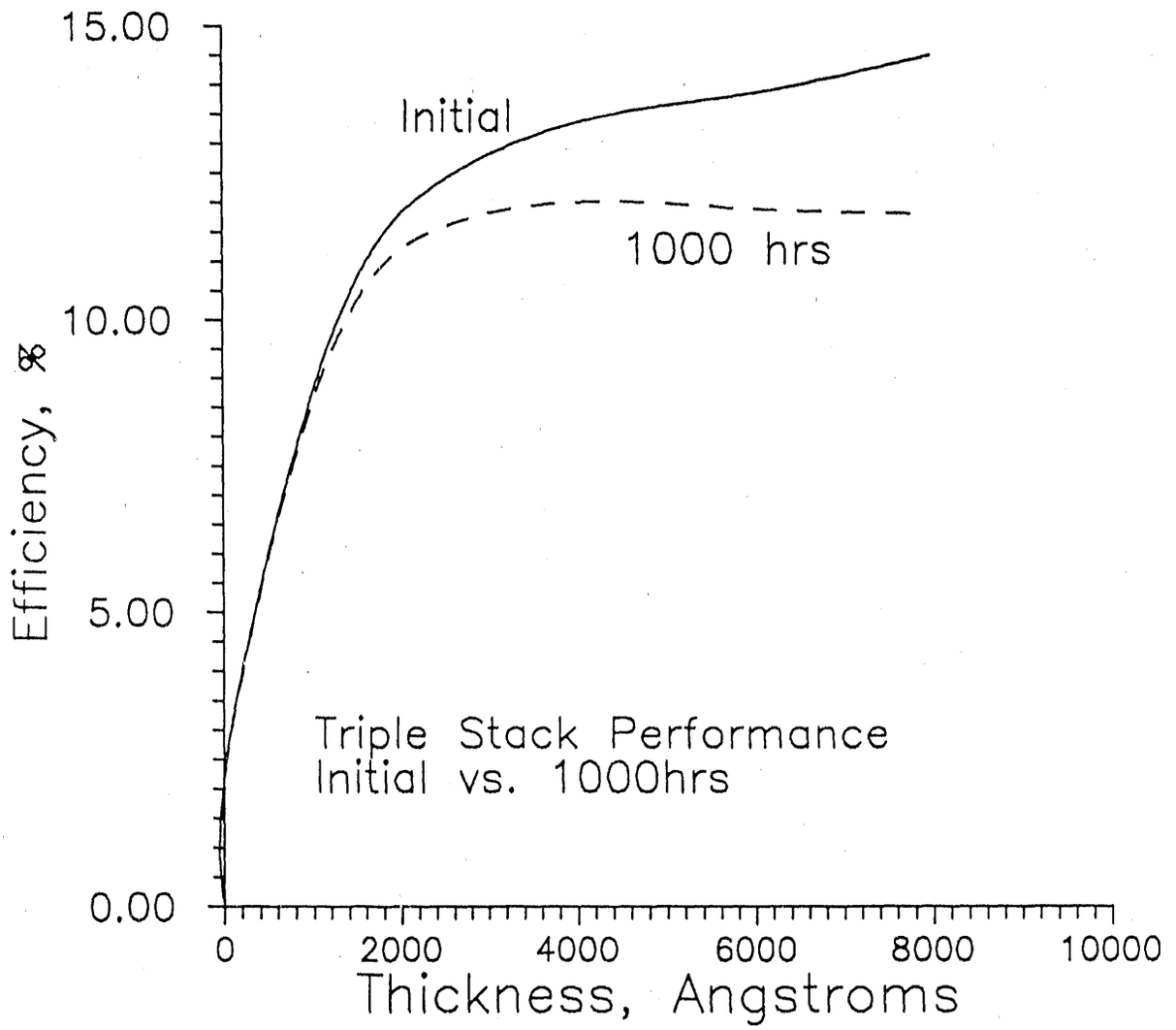

Although after 1000 hrs. exposure, the decrease of the initial conversion efficiency is larger the greater the i_2 layer thickness, the model suggests that the final stabilized efficiencies are nearly independent of thickness for $i_2 > 4000$Å. Unlike single junction devices, the long-term performance of the module should be virtually independent of the design as shown in **Figure 2-9**.

2.5 MICROCRYSTALLINE SI FORMED BY RAPID THERMAL ANNEAL

Due to the need for highly conductive doped layers which also offer as little optical absorption as possible, several new methods for producing microcrystalline silicon have been explored. The formation of microcrystalline silicon by plasma deposition has been described in previous reports to SERI, and has generally been difficult to accomplish in layers thinner than 200Å, as would be required for the doped layers of an a-Si based solar cell. One new deposition method which has shown promise is the formation of thin microcrystalline silicon by rapid thermal anneal (RTA) of a previously deposited a-Si layer.

Several samples of microcrystalline Si were produced using this approach. Thick samples of a-Si (about 2000Å) which had been either undoped, boron doped, or phosphorus doped were plasma deposited on quartz substrates. Subsequent rapid thermal anneal of these samples for times as short as four minutes yielded the most highly conductive microcrystalline films ever measured at Solarex, on the order of 200 $(\text{ohm-cm})^{-1}$. Moreover, a very high conductivity was retained even in thin (200Å) films produced using the same technique for both p+ and n+ doped silicon (See **Figure 2-10**). In contrast, microcrystalline films which are produced by direct plasma deposition have never exhibited as high a conductivity in thin layers (see **Figure 2-11**). The high degree of crystallinity was confirmed by Raman spectroscopy for both thick and thin layers, however, an additional Raman signal is present in the case of the thin film spectra which is probably due to silicide formation with a nichrome pad between the silicon sample and the quartz substrate, required for conductivity measurement. Unfortunately, the Raman signal for the 200Å films is not accurate over areas in which the silicon was directly on the quartz due to the large Raman signal from the underlying quartz itself. An increase in optical transparency at short visible wavelengths due to the amorphous to microcrystalline transition is also evident as expected (see **Figure 2-12**).

It is speculated that highly conductive microcrystalline Si could not easily be formed in very thin layers by direct plasma deposition because the growth processes are isotropic, thus limiting the crystallite grain size to the thickness of the film or less. On the other hand, formation of microcrystalline Si via subsequent RTA of a very thin film could well be an anisotropic process, yielding large, flat microcrystallites whose size is limited by the film thickness in only one

Figure 2-10. Arrhenius plot of the conductivity of thin (200Å) silicon films before and after crystallization by rapid thermal anneal (RTA). Both p-type and n-type films are shown.

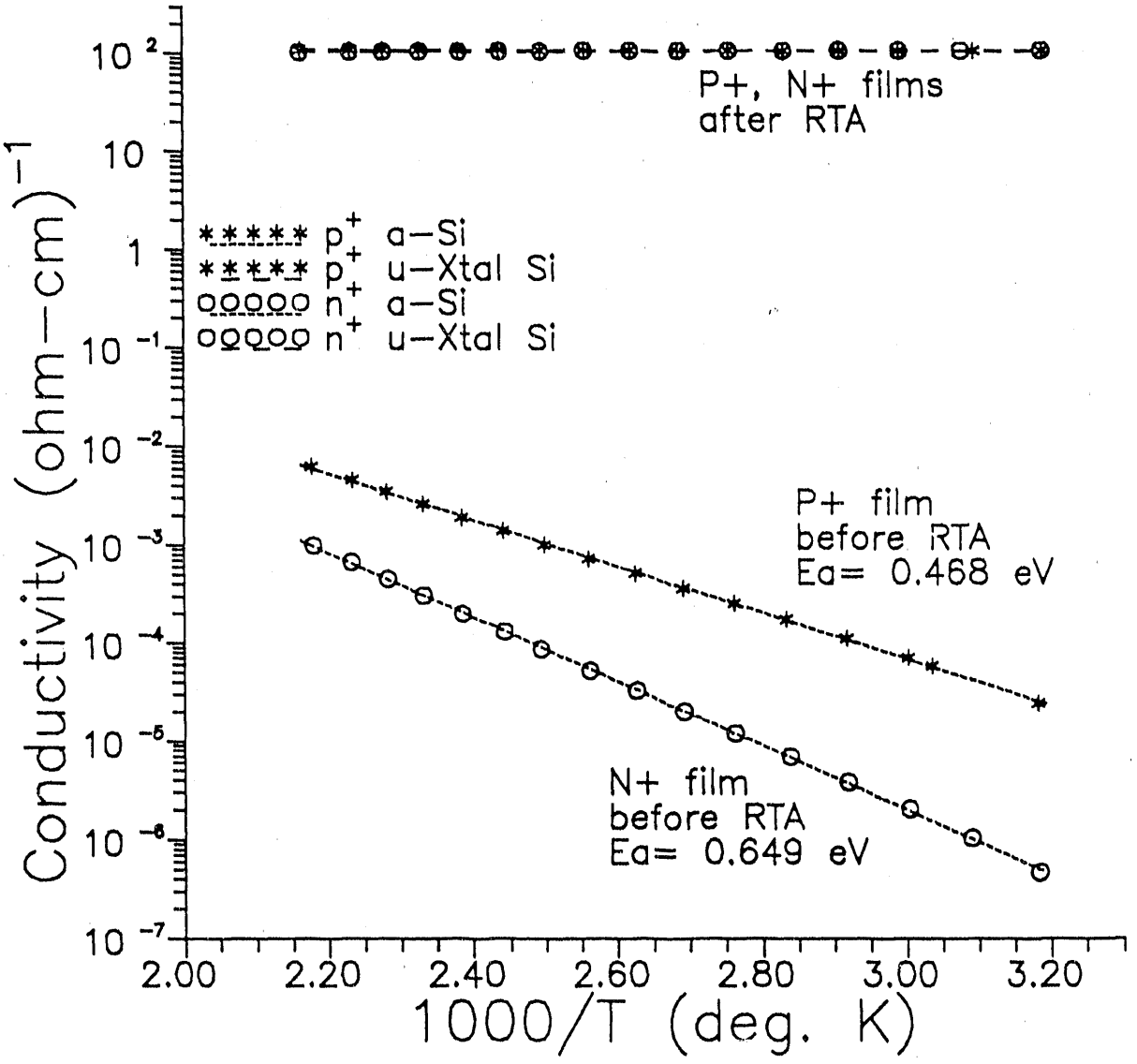

Figure 2-11. Plot of the dependence of conductivity on film thickness. Typically, the conductivity decreases rapidly as thickness decreases below about 800Å for material which is plasma deposited under "microcrystalline growth" conditions. Exceptional behavior is exhibited for the films crystallized by RTA, as shown.

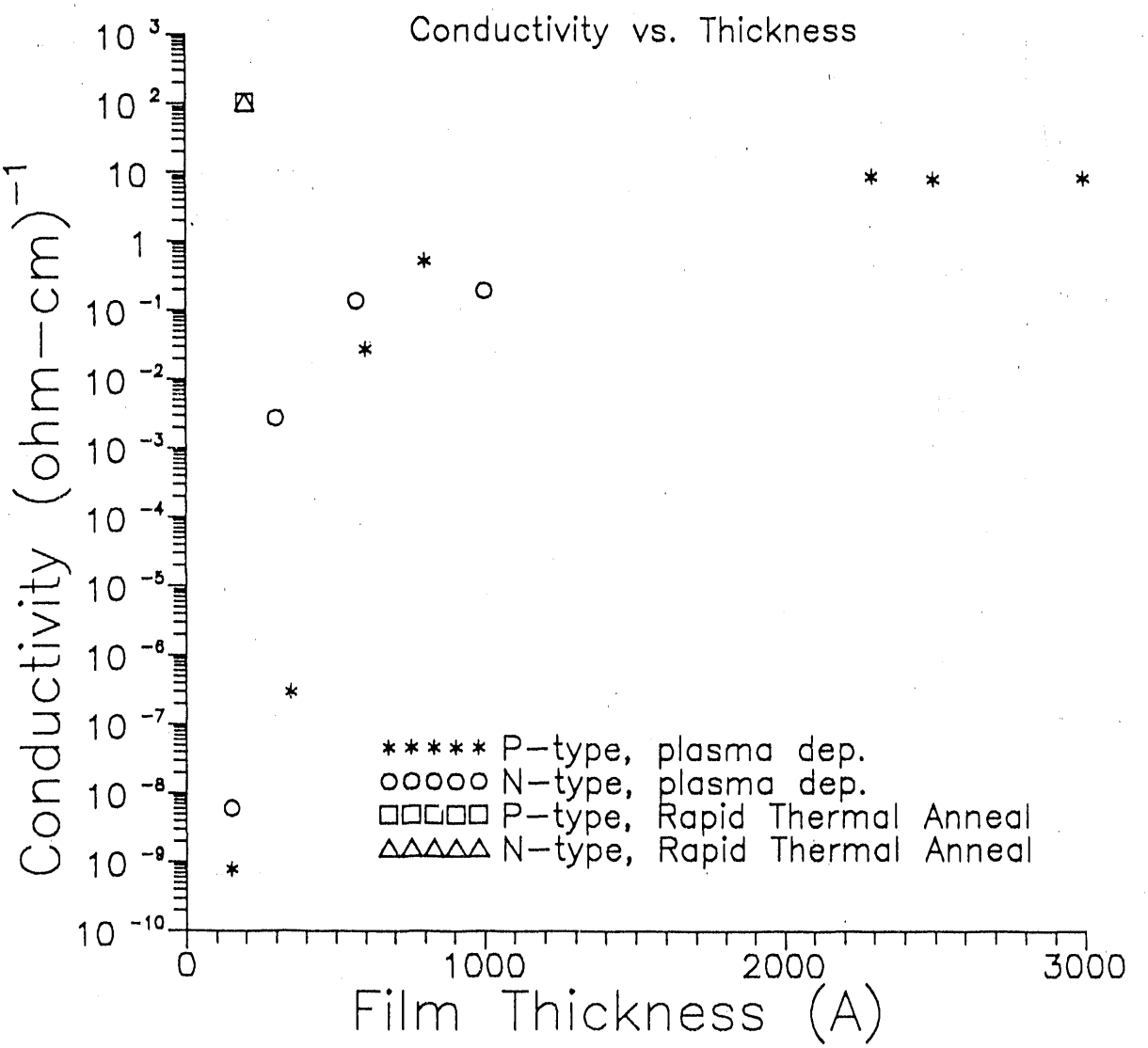

Figure 2-12. Optical transmission measurements of a p-type silicon film before and after crystallization via RTA. A noticeable decrease in the optical absorption coefficient, as expected for μ-xtal vs. amorphous material, is evidenced as greater optical transparency in the 400 to 600nm range.

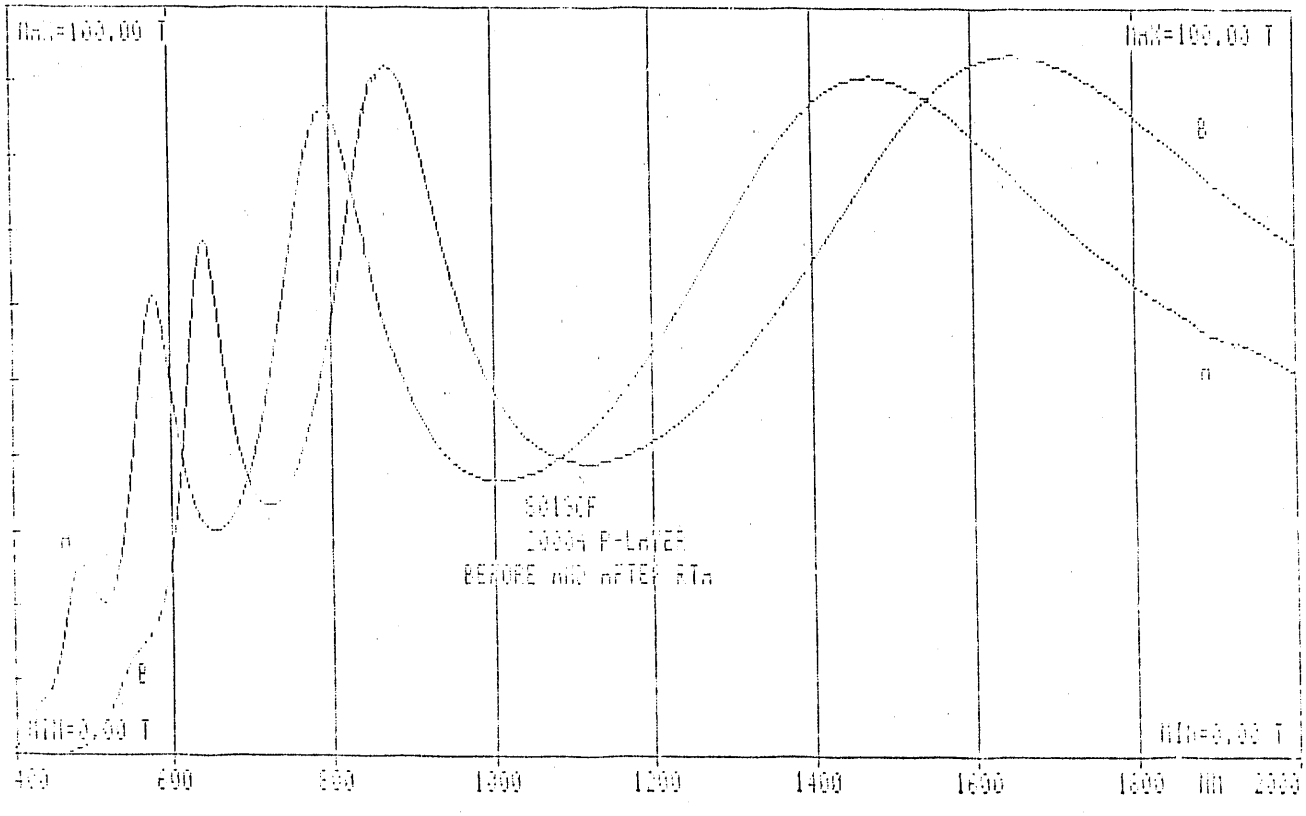

dimension. Some evidence was obtained recently by transmission electron microscopy which indicated that, indeed, the grain size of the microcrystallites in the silicon films produced by RTA of a-Si are much larger than the thickness of the film itself (14).

Thus, this method is capable of producing very thin, highly conductive layers of either p+ or n+ type microcrystalline silicon on a foreign substrate with a lower optical absorption coefficient than a-Si. All of the material requirements for use in devices are satisfied. Single junction p-i-n devices were made using a p+ layer consisting of silicon which had been microcrystallized using the RTA technique, but did not perform well probably due to problems at the p+-i interface. The cause of these problems was suspected to be formation of an oxide or contamination layer at the surface of the p+ layer either during the RTA treatment, or during transfer between the RTA apparatus and the a-Si deposition apparatus. Two separate systems required to test the entire RTA process in a p-i-n device format. Transport in atmospheric ambient of the partially completed device was required between the first (plasma deposition) apparatus to the second (RTA) apparatus, and then back again to finish plasma deposition of the intrinsic and n+ layers. Oxide formation or contamination likely occurred during the time that the sample was transferred from the deposition apparatus to the RTA apparatus, and then back again to the deposition apparatus. Oxide contamination could also have been introduced during the RTA process itself, because this exposes the surface of the p+ layer at high temperature (700°C) to a gas ambient which likely contains oxygen at low levels. A reducing atmosphere would be preferred for this operation, but due to safety concerns the RTA had to be carried out in a hydrogen/nitrogen gas mixture which is below the flammability limit (~2% hydrogen) in this particular RTA apparatus.

Several wet chemical and dry plasma treatments were used in an attempt to remove any oxide contamination layer from the surface of the microcrystalline p+ layer before completion of the device by deposition of the i-n+ layers. These included wet etching of the p+ layer after RTA in 5% and 10% HF in de-ionized H_20 and in methanol, buffered oxide etchant (HF in ammonium fluoride solution), and hydrogen plasma etches after reintroduction into the deposition chamber.

Various combinations of these oxide removal steps improved the device performance significantly, but did not yield device performance better than that available using a standard, all plasma deposited p-i-n cell. In order to properly evaluate the technique, it would be necessary to set up the means for effecting an RTA within the plasma deposition apparatus. In this way an RTA could be included on the p+ layer to convert it to highly conductive, microcrystalline silicon in a fully reducing gas ambient and the remainder of the device could be completed without atmospheric exposure, thus avoiding contamination at the p+/i interface.

3.0 NON-SEMICONDUCTOR MATERIALS RESEARCH

3.1 ATMOSPHERIC AND LOW PRESSURE CVD (LPCVD) OF ZNO

Although textured tin oxide is currently used as a front contact layer for solar cells and modules, optical analysis of the amorphous silicon multi-junction structure indicates that the non-semiconductor materials used in the solar cell accounts for the most significant optical losses. Efforts to reduce the optical loss are centered around minimizing optical absorption and increasing light scattering while improving the electrical conductivity of the layers using ZnO.

Doped zinc oxide (ZnO) films were prepared and studied as transparent contacts in photovoltaic devices. The primary objective was to improve upon on the electrical conductivity and optical transparency of doped tin oxide (SnO_2) films which are presently used in device fabrication. Less optical absorption in the blue region of the spectra is expected from zinc oxide films because they have a larger band gap (3.2 eV) compared with the band gap obtained with tin oxide films, (3.0 eV) (15). Doped zinc oxide is a more versatile contact because it can be deposited at lower temperatures, (below 200°C) while SnO_2 requires deposition temperatures over 300°C (16). We have been able to use zinc oxide films not only as a front contact on glass, but also as a back contact on amorphous silicon and $CuInSe_2$ cells where deposition temperatures are limited by the requirement that the underlying device not be thermally degraded. A secondary advantage of zinc oxide as a metal oxide conductor is that it is etched easily with dilute acid while tin oxide requires much more vigorous etching conditions. Zinc oxide is more resistant to reduction by the hydrogen plasma encountered during a-Si deposition yielding a more optically transparent window in devices.

There are many techniques such as sputtering for depositing zinc oxide films (17). Because of the promising results of others (18-20), we investigated chemical vapor deposition (CVD) of diethylzinc (DEZ) and water as follows:

$$\begin{aligned} Zn\,(CH_2CH_3)_2 \;+\; 2H_2O &\rightarrow Zn\,(OH)_2 \;+\; 2\,C_2H_6 \\ Zn\,(OH)_2 \;+\; heat &\rightarrow ZnO + H_2O \end{aligned} \qquad (12)$$

The deposition is a complex reaction with both gas phase and surface reactions. Diethylzinc is a commercially available pyrophoric liquid (boiling point 118°C) that is thermally stable in the absence of air. Conductivity of the zinc oxide film is increased by adding a dopant such as boron or aluminum to the deposition feedstocks.

Initial studies were carried out by atmospheric CVD using the apparatus pictured in **Figure 3-1**. The deposition system consisted of metal bubblers cooled to slightly below room temperature. The bubblers were fed a nitrogen carrier gas with precise levels of water vapor and DEZ vapor determined by the bubbler temperature and the vapor pressure of the liquid. The reactants, along with the dopant and nitrogen diluent, were mixed and passed over a heated 3 x 3 inch glass substrate. An aluminum block with a cylindrical heating element embedded in it was used to uniformly heat the substrate.

Depositions were made on the apparatus using various mixing chambers and gas inlets. Substrate temperature, dopant levels, DEZ flow, water vapor flow, and diluent nitrogen flow were systematically varied to prepare different films. Hydrogen fluoride, trimethylboron, and diborane were examined as dopants. Diborane gave material with the lowest resistance. Atmospheric CVD produced both specular and textured films with thicknesses of 0.5 to 3 microns. Film resistances as low as 10 ohm/sq (conductivities of 500 $(ohm\text{-}cm)^{-1}$) were obtained. Typical deposition rates were 300-500 Angstroms per minute. The apparatus demonstrated the feasibility of atmospheric pressure CVD of zinc oxide. Conductive zinc oxide was prepared that met the optical and electrical requirements for photovoltaic devices. The major area requiring improvement was sample uniformity. Despite the investigation of a wide range of gas inlet geometries and gas mixing chambers, it was not possible to obtain optically uniform samples on 3 x 3 inch substrates.

One approach used to prepare more uniform samples is low pressure chemical vapor deposition (LPCVD) of zinc oxide from DEZ vapor and water vapor. **Figure 3-2** shows the apparatus that was built using a glass bell jar with a metal gas mixing chamber. A rotary vacuum pump with a pressure controller was used to maintain deposition pressures between .5 to 5 torr. The bubblers were heated in an ethylene glycol bath at 45° to 75°C depending upon the desired reactant concentration. All lines with water or DEZ vapor were heated to well above the bubbler temperature to prevent the condensation of reactants. The reproduceability of the zinc oxide depositions was highly dependent on proper control of line temperatures.

Because the films prepared by LPCVD gave more uniform films compared to atmospheric deposition pressure, it was possible to assess the effects of changing deposition conditions. The major variables examined were the same as those for atmospheric pressure CVD studies, (substrate temperature, dopant level, DEZ flow, water vapor flow, and diluent nitrogen flow), with the addition of pressure. **Figure 3-3** shows that the ZnO film growth rate increases

Figure 3-1. Apparatus for the atmospheric deposition of zinc oxide from water and diethylzinc vapor.

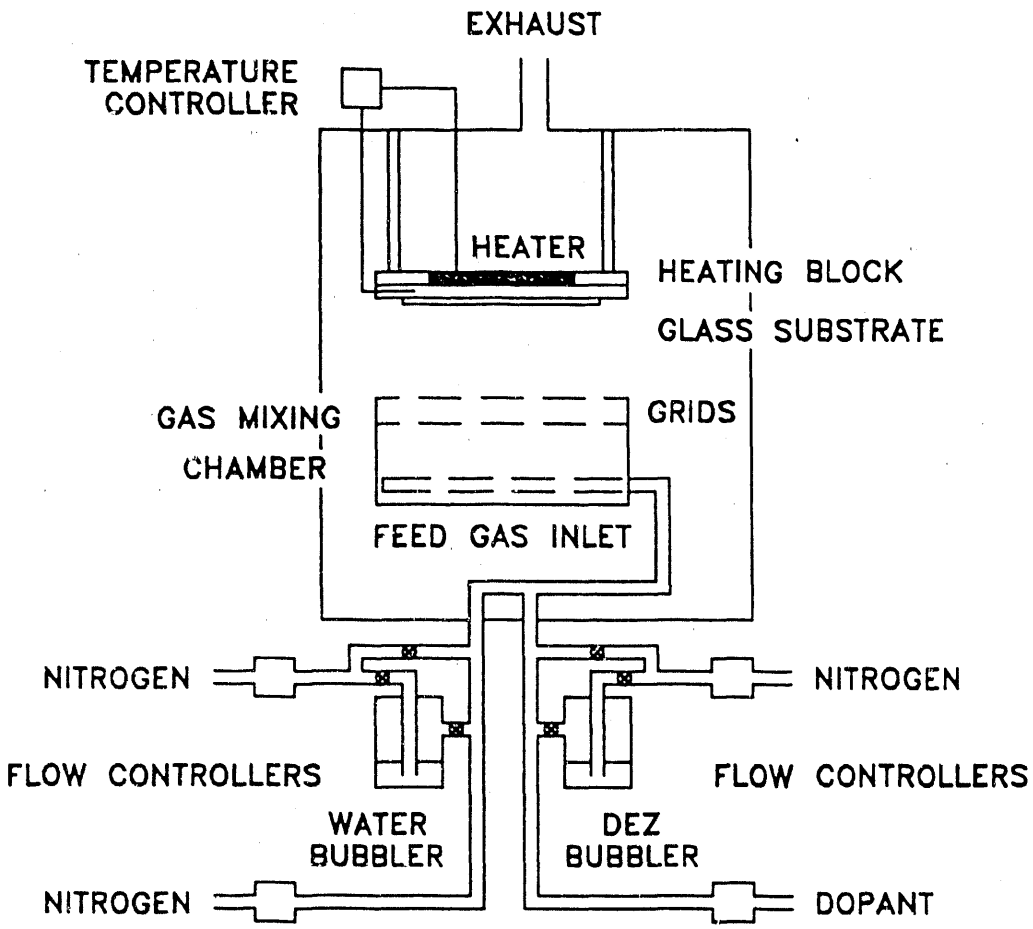

Figure 3-2. Apparatus for the low pressure deposition of zinc oxide.

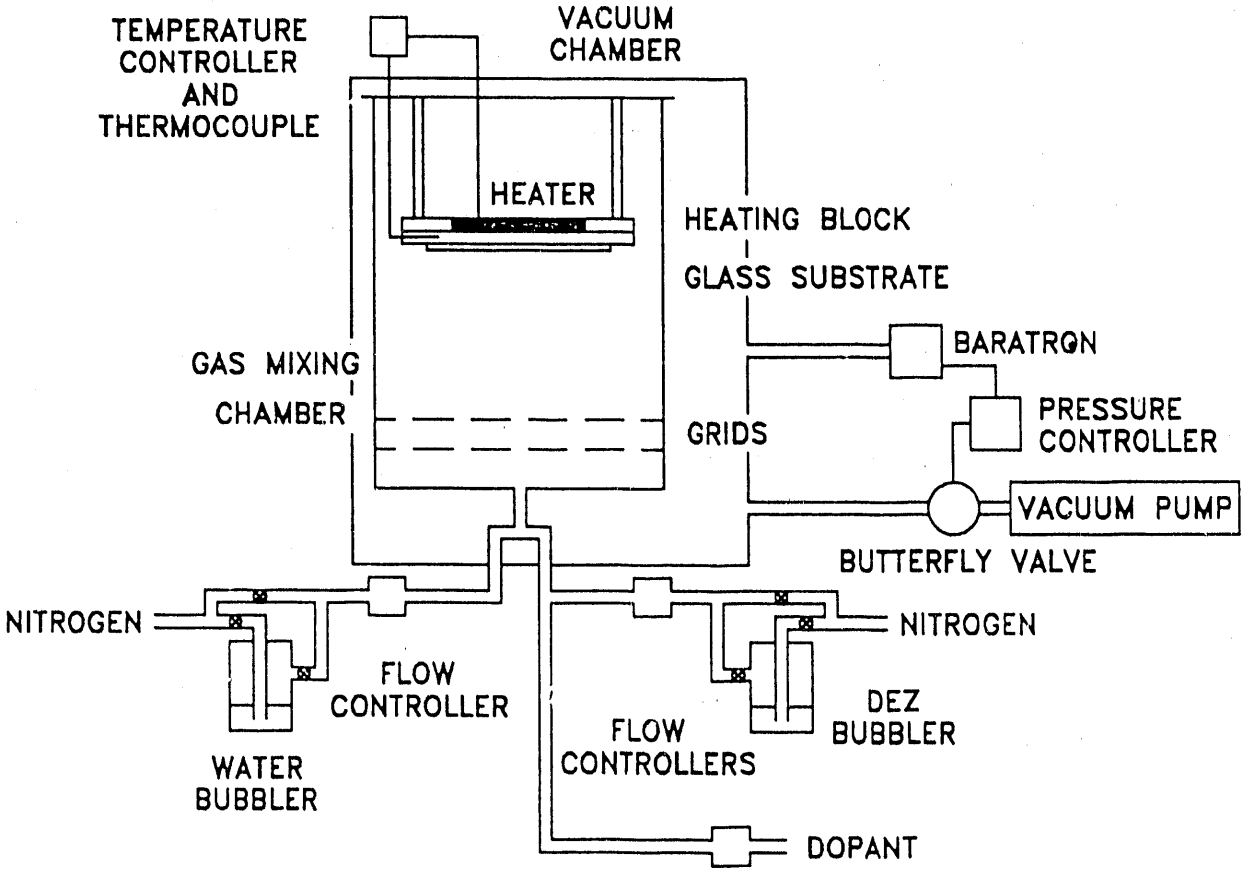

Figure 3-3. Growth rate of zinc oxide films from diethylzinc and water by low pressure vapor deposition as a function of temperature.

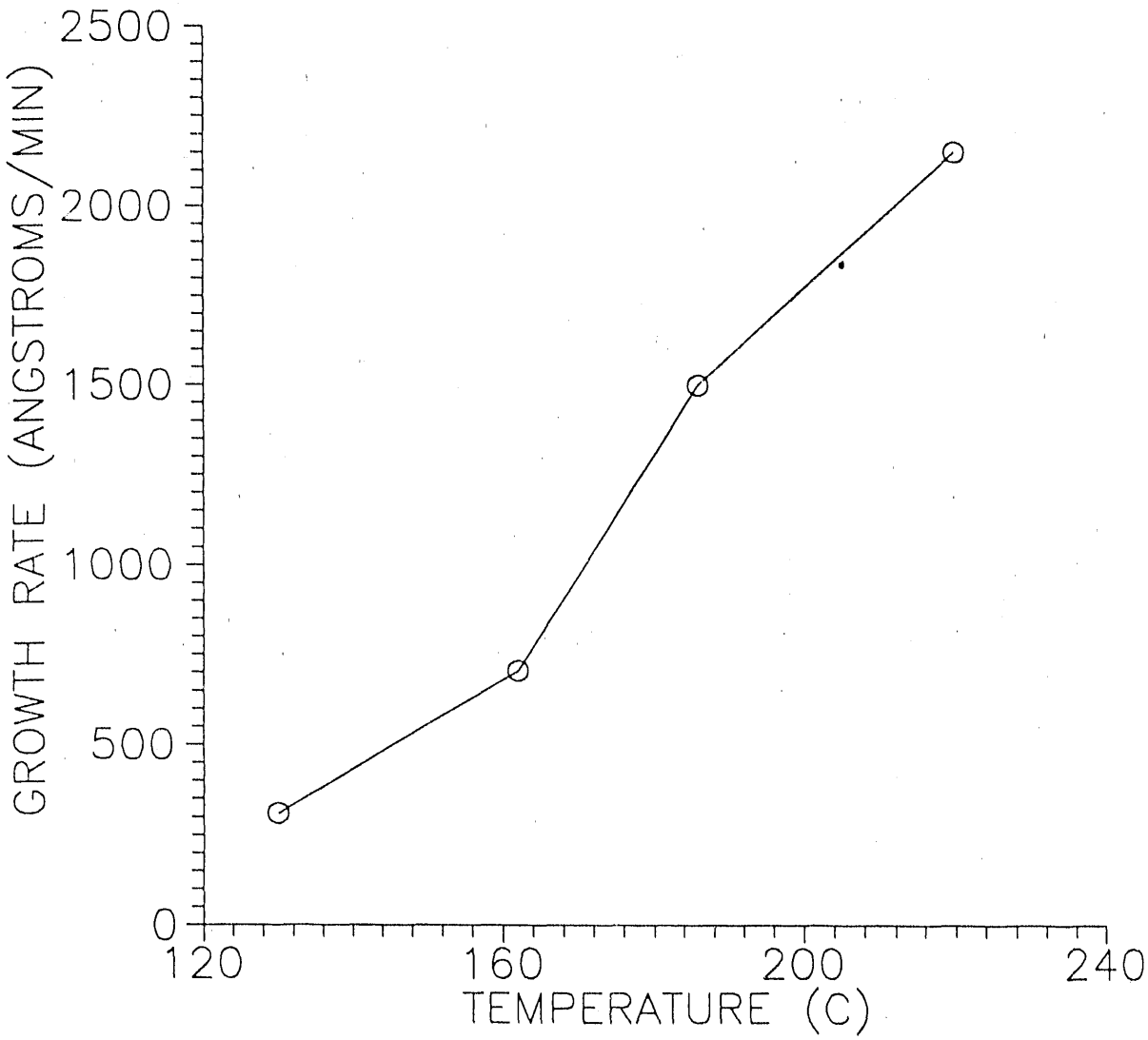

rapidly with temperature. **Figure 3-4** shows that doping with diborane is a complex function of diborane concentration. As the diborane flow is increased, resistance decreases rapidly and then slowly increases. The decrease in conductivity at high dopant concentration is consistent with the lower mobiity expected for ionizing impurity scattering. **Figure 3-5** shows the relationship between film thickness and resistance (ohm/sq).

Under the best conditions films were prepared on 3 x 3 inch substrates with a thickness that varied by less than $\pm$ 0.05 microns. The transmission had a spacial variations of less than 0.5%, and conductivities of 11 $\pm$ 1.0 ohm/sq were measured.

Table 3-1 gives a sampling of the types of films prepared. Uniform 3 x 3 inch films ranging from very transparent specular films to highly textured films were prepared with good conductivities and transmissions. The haze and transmission values were obtained using a Gardner (Silver Springs, MD) XL-211 Hazegard hazemeter and reflect average values over the visible spectrum. Conductivity measurements were obtained using the standard four-probe method.

Table 3-1

Electrical and Optical Properties of Typical ZnO Films Prepared by CVD

Sample #	Thickness (microns)	Resistance (ohm/sq)	Conductivity (1/(ohm-cm)	Transmission (%)	Haze (%)
606	1.0	35	290	87.0	0.4
655	1.1	27	340	86.8	6.7
650	1.6	11	570	84.6	9.2
647	1.5	23	290	84.7	17.9
645	1.5	12	560	83.5	25.6

Figures 3-6 through **3-8** give the transmission and reflectance spectra of typical films as one progresses from specular (**Figure 3-6**) to textured films (**Figure 3-8**). The higher optical absorption found for the textured films is the result of incident light being scattered out of the path of the primary beam of the spectrophometer, and internal trapping.

Figure 3-4. Resistance (ohm/sq) in zinc oxide films of similar thicknesses as a function of dopant (trimethylboron) flow.

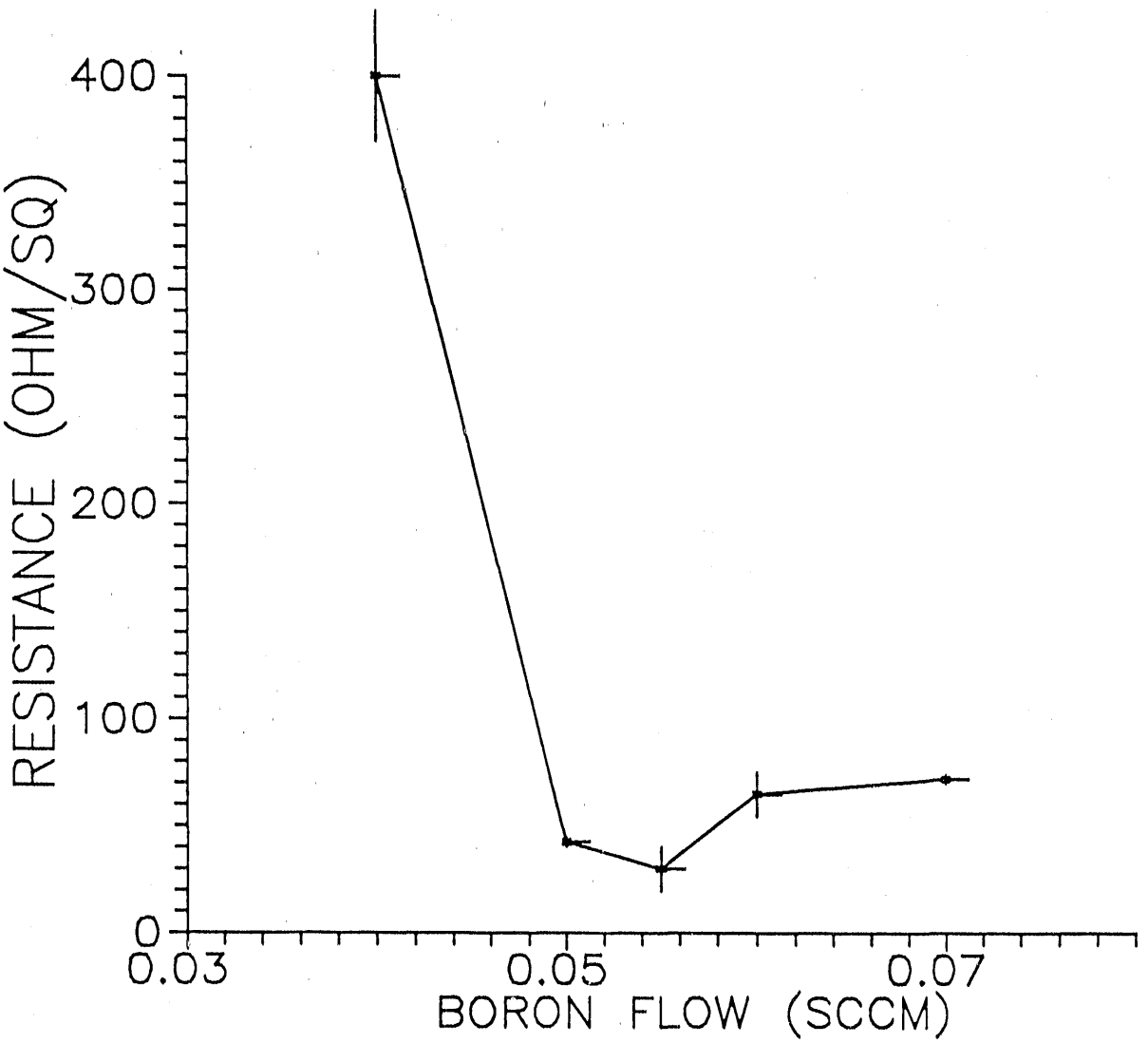

Figure 3-5. Dependence of zinc oxide film resistance on film thickness.

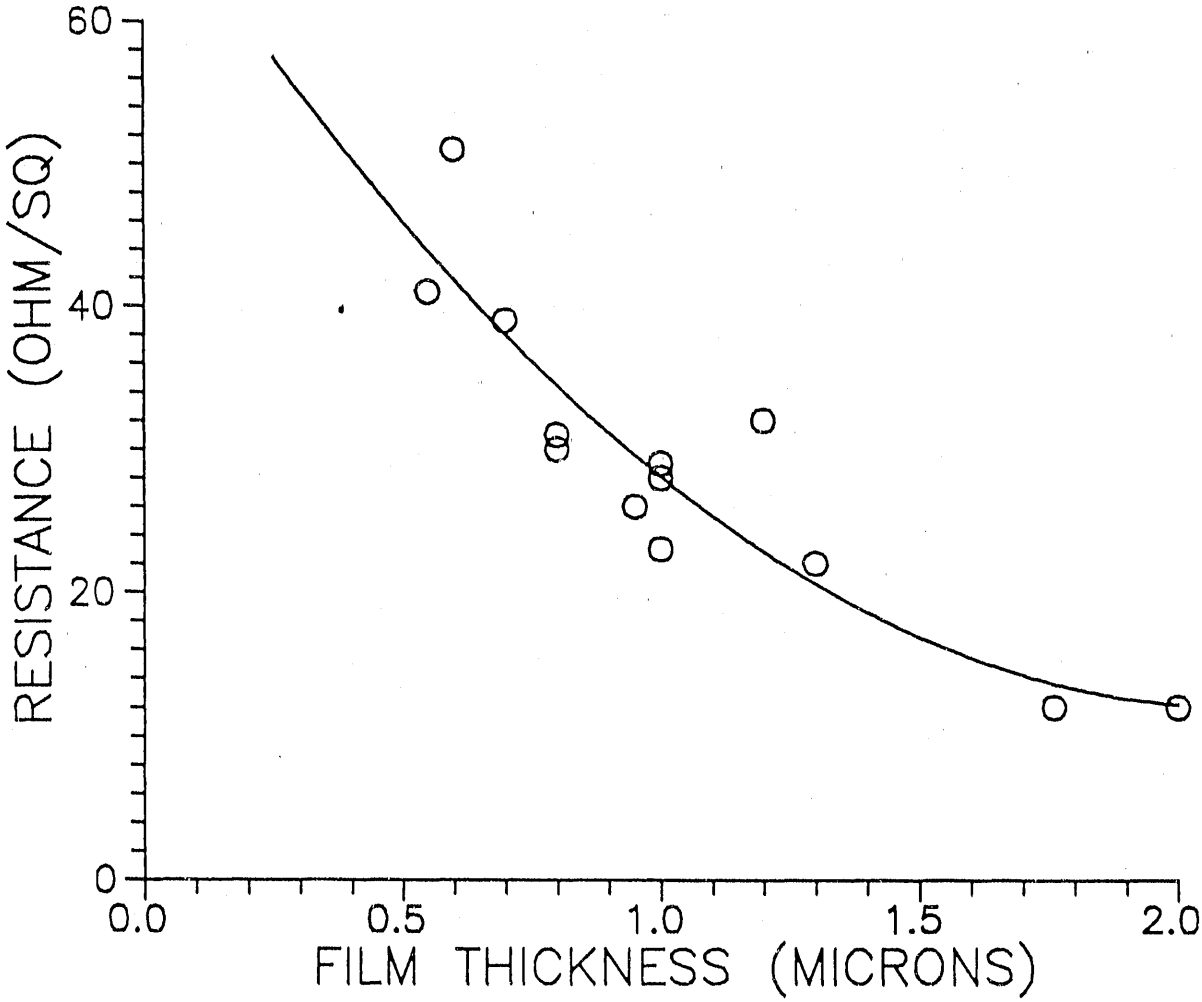

Figure 3-6. Transmission and reflectance spectra of a specular (haze of 0.3%) film of zinc oxide.

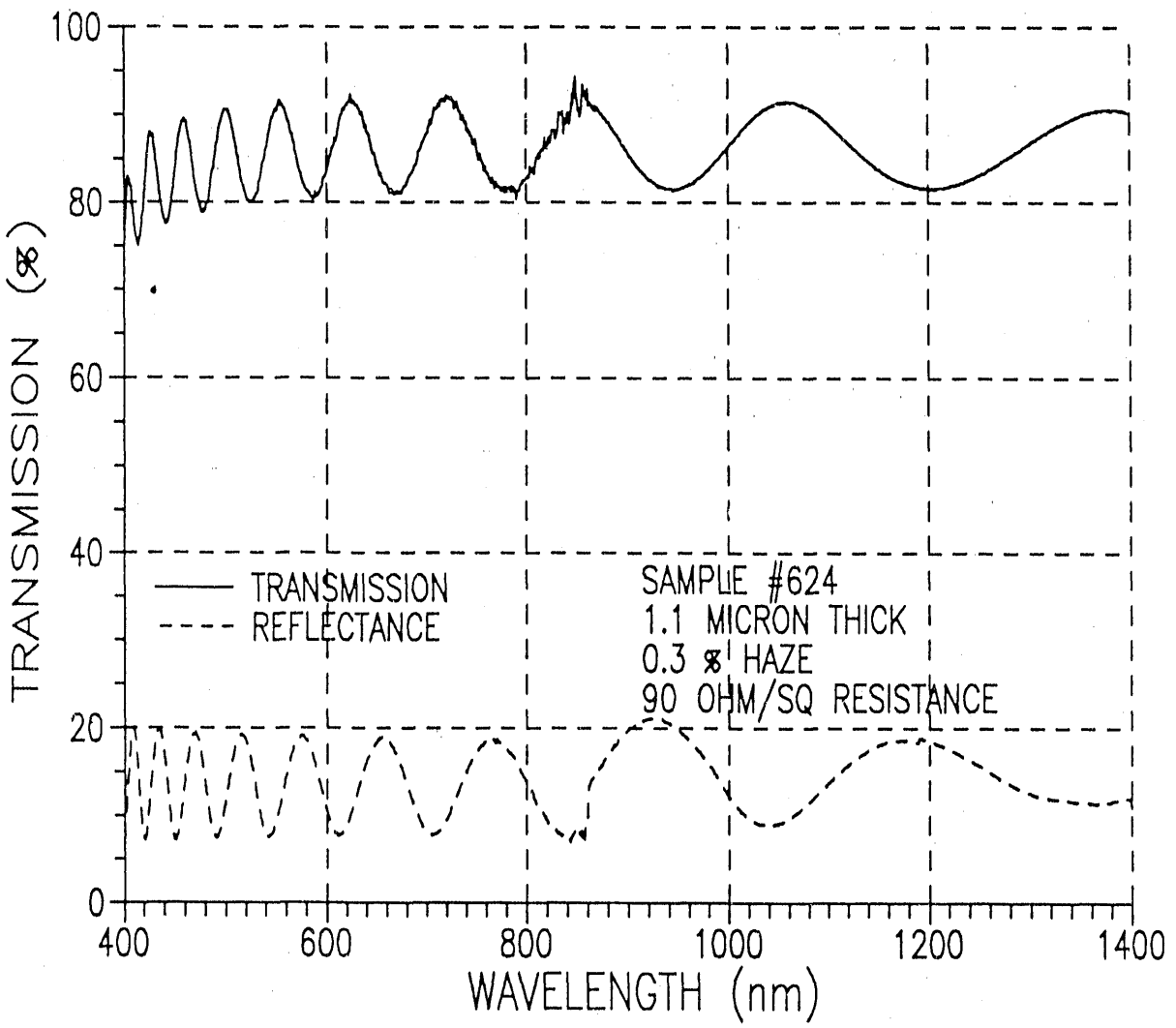

Figure 3-7. Transmission and reflectance spectra of a slightly textured (haze of 6.1%) film of zinc oxide.

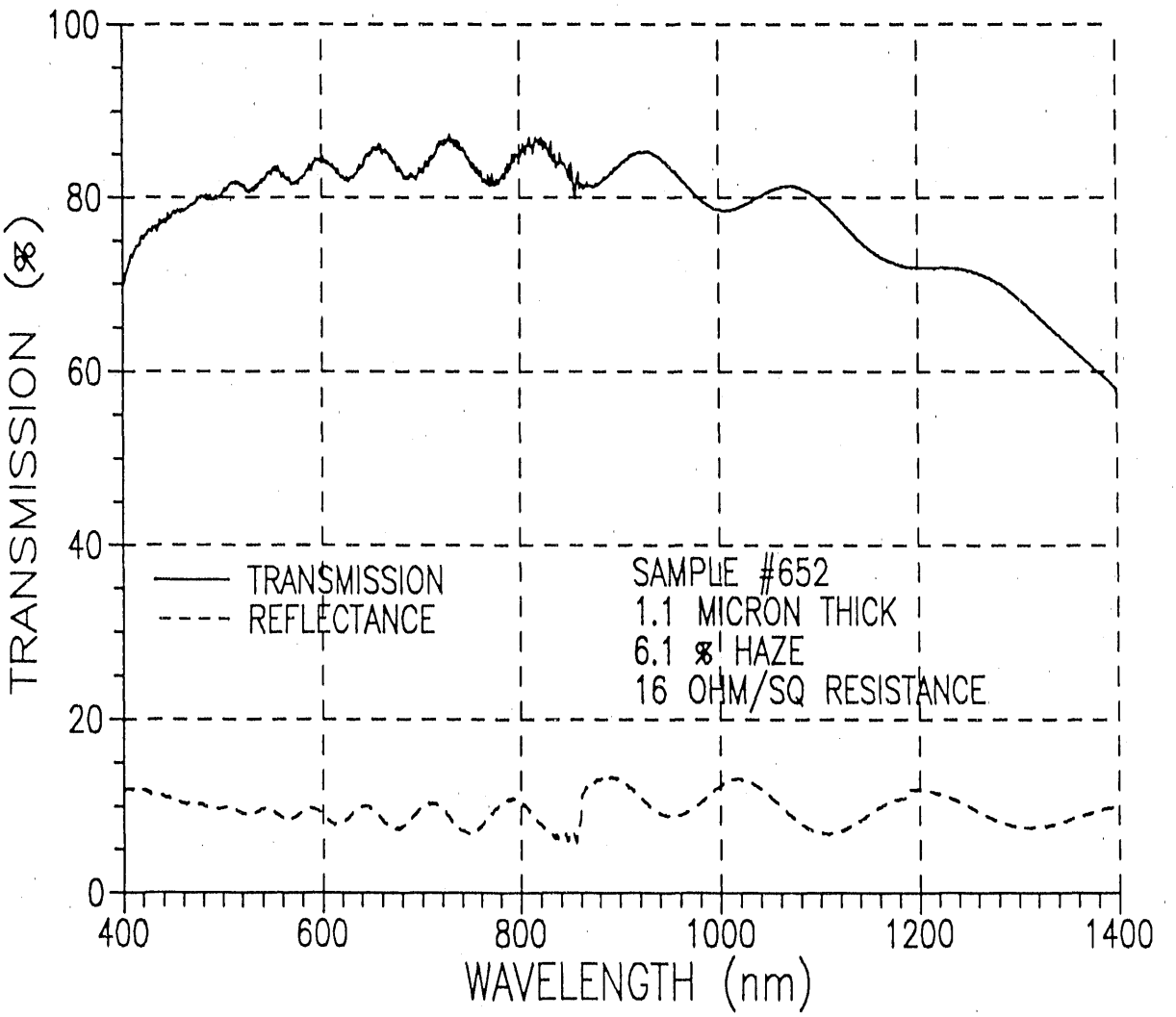

Figure 3-8. Transmission and reflectance spectra of a textured (haze of 17.9%) film of zinc oxide.

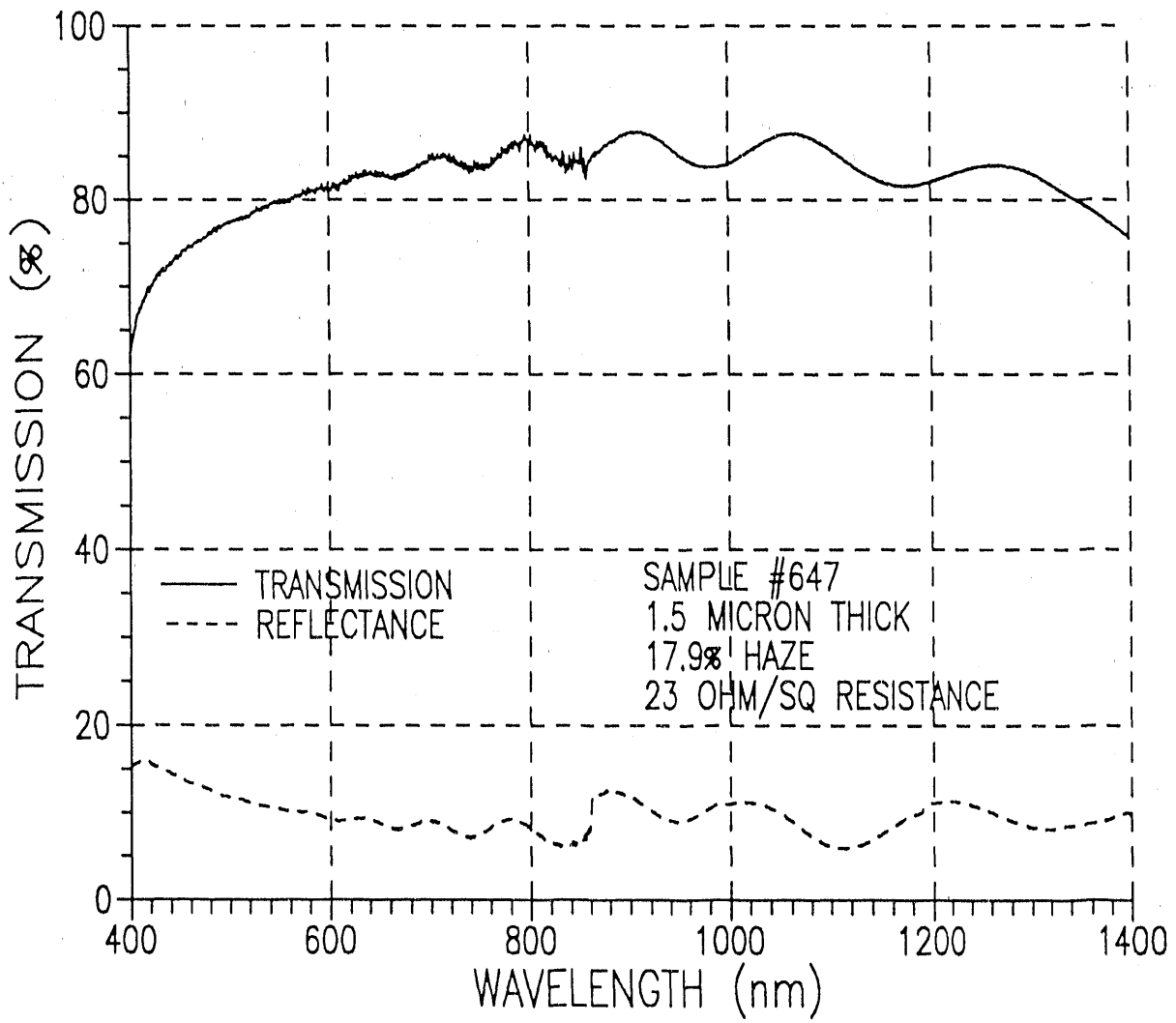

Films with a wide range of textures have been prepared. Such films had good adhesion to glass, a-Si:H, and other substrates. Specular zinc oxide films, however, showed a tendency to peel. Factors such as deposition temperature and rate of cooling had no effect on the adhesion. The thinner films generally had better adhesion. Specular zinc oxide films greater than about two microns readily detached from glass, especially if the glass was brought in contact with water or etchant. Films of specular zinc oxide over about one micron in thickness peeled off of a substrate coated with a-Si:H. Based on scanning electron micrographs (SEM) (19), one likely explanation is that the structure of textured zinc oxide, made up of many small particles, can absorb internal stresses more readily than the uniform specular films.

Work has begun on preparing a-Si cells on the zinc oxide films. Initial studies indicate some kind of post deposition treatment of the zinc oxide film will be required. The zinc oxide films give an excellent red response but yield a poor fill factor and open circuit voltage. Tin oxide coated glass run at the same time gave similar results indicating contamination of the glow discharge by the ZnO film.

3.2 SPUTTERED ZINC OXIDE FILMS

Indium-tin-oxide (ITO), in combination with silver metal, is presently employed as a high reflectivity rear contact for solar cells and modules. We have investigated the use of a zinc oxide layer as a lower cost alternative to the ITO layer in the rear contact. Zinc oxide films have been prepared by sputtering over areas larger than 900 cm^2 using two forms of starting material. Highly transparent, conducting zinc oxide films have been deposited from metallic targets and from zinc oxide/aluminum oxide targets. Optical transmissions in the range of 80 to 85% with sheet resistances of 200-1000 ohms/square on 1000Å thick films have been achieved.

Figures 3-9 and **3-10** show the current-voltage and quantum efficiency measurements of a single junction solar cell with a zinc oxide/silver rear reflecting contact. The fill factor and long wavelength response of this device is comparable to those expected for a similar solar cell with an ITO/silver reflector.

3.3 ALTERNATE REAR REFLECTORS

A program of research has begun to further minimize optical losses due to absorption at the rear contact. Optical modeling has indicated that this loss amounts to about 4 mA/cm^2 in a typical triple stack cell using ITO/Ag as the rear contact. Although, on theoretical grounds, the reflectivity of ITO/Ag would be expected to be very good, the measured reflectivity of a textured

Figure 3-9. Current - voltage curve of single junction solar cell with zinc oxide/silver rear contact.

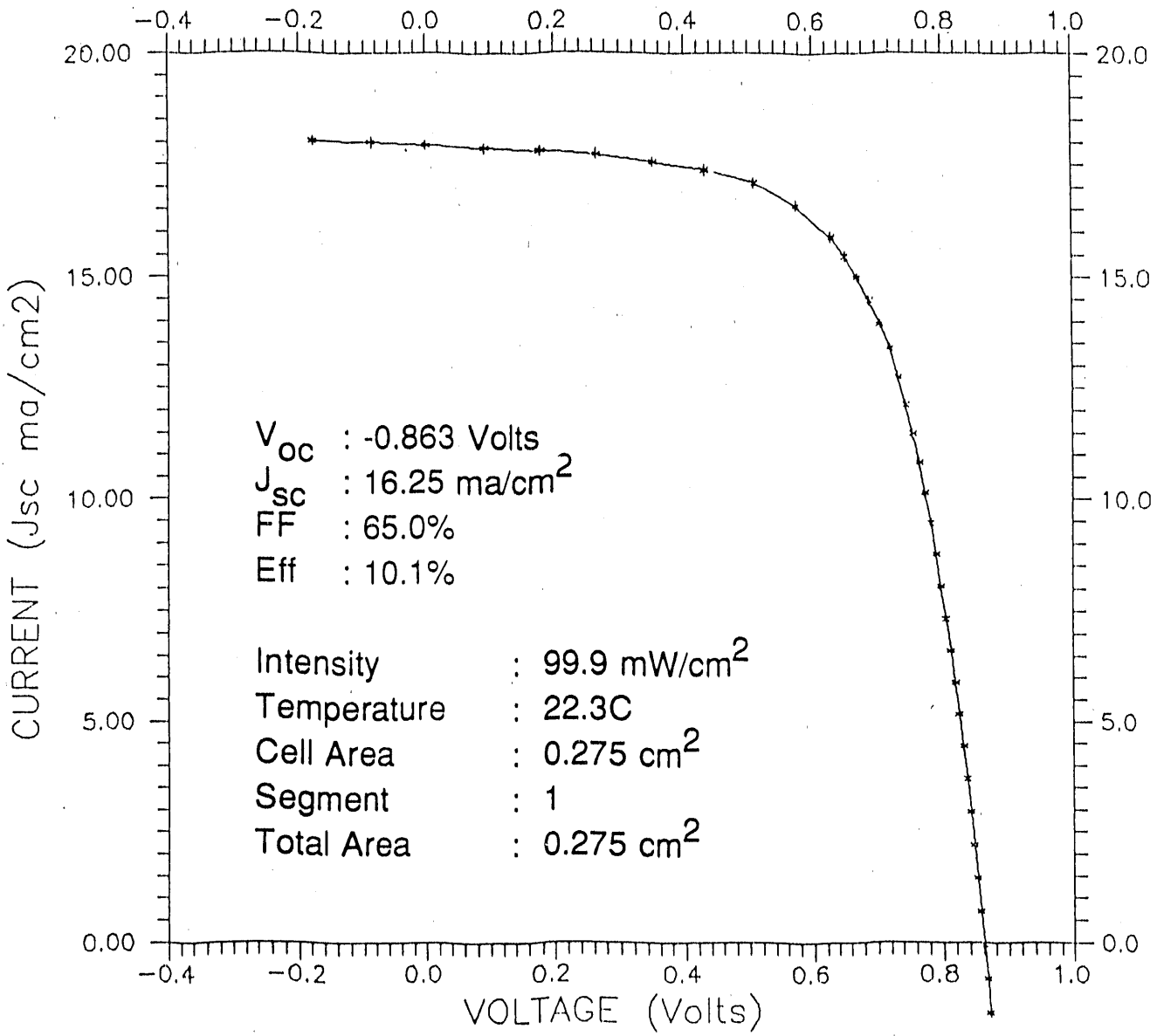

Figure 3-10. Quantum efficiency of single junction solar cell with zinc oxide/silver rear contact.

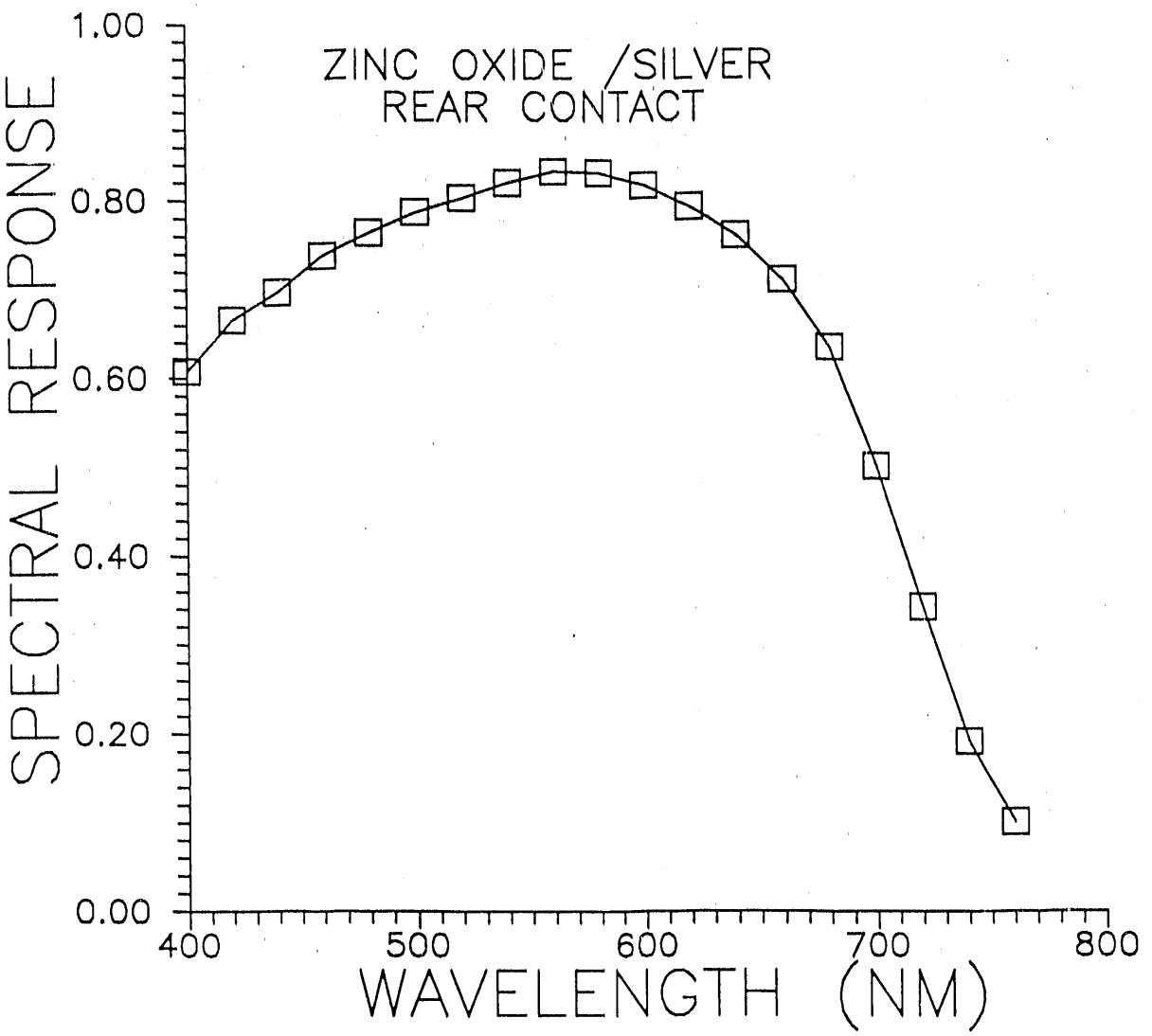

ITO/Ag interface rises only to about 70%-75% in the red-infrared. This reduced reflectivity is believed to arise from the formation of an optically absorbing interface layer between the silver and the ITO, perhaps silver oxide. The effects of texturing are expected to exacerbate any loss of reflectivity due to multiple bounce phenomena at the ITO/Ag textured interface. One possible solution to this problem is the use of a very thin layer of material in between the ITO and Ag which would act as a "diffusion layer", preventing any reaction between the ITO and silver which might form an optically absorbing compound. One material which has been evaluated for use as a "diffusion barrier" has shown promise by raising the reflectivity of the ITO/Ag reflector from about 70% to better than 95% (both numbers adjusted for optical trapping in the measurement structure, see **Figure 3-11**). This material, as well as several other materials, will be further evaluated with intent to reduce the rear contact optical loss.

Figure 3-11. Measured reflectivity (after correction for light-trapping effects) of a standard (ITO/Ag) textured reflector and an improved reflector under development at Solarex.

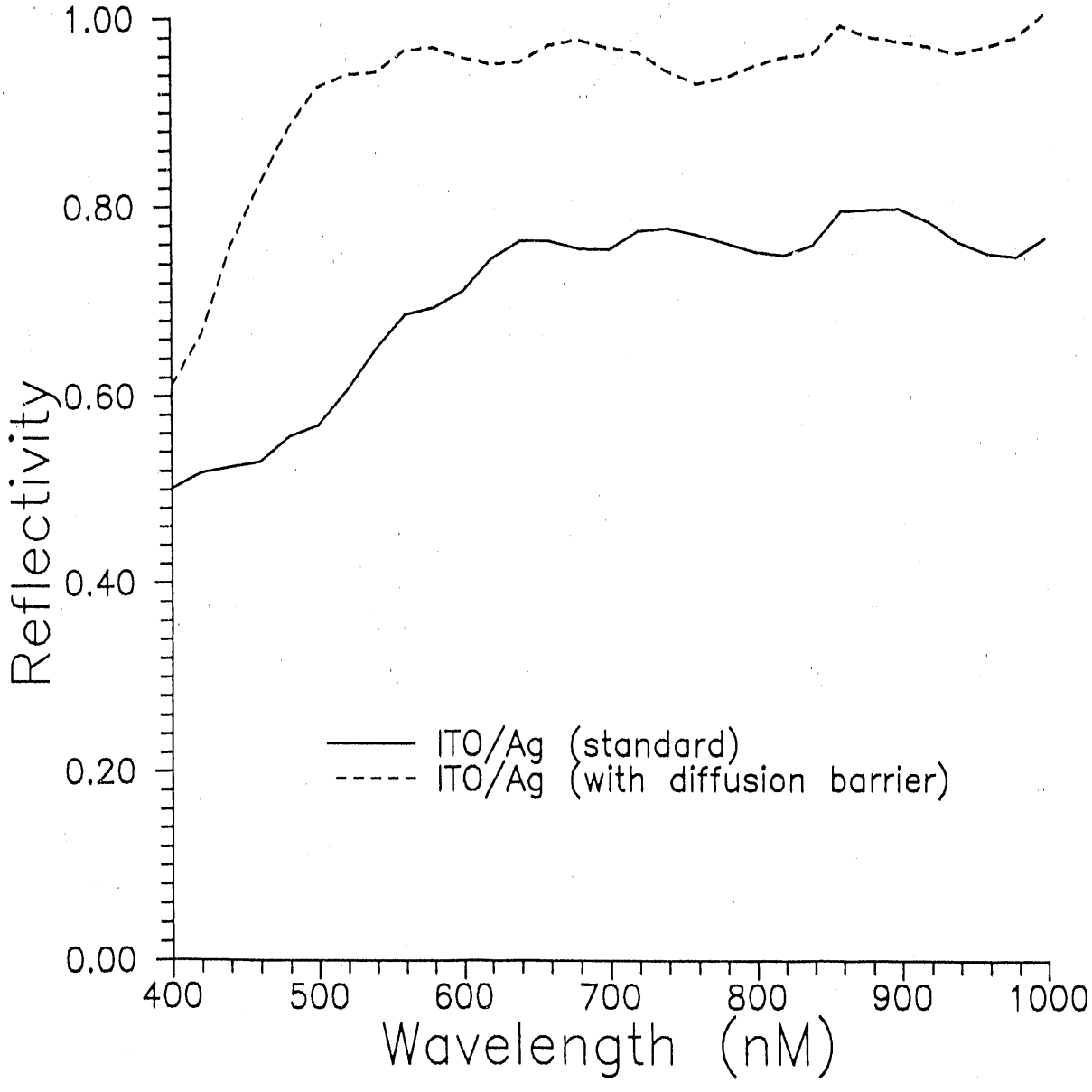

4.0 SUBMODULE RESEARCH

4.1 INTRODUCTION

The principal first year goal of this task is the development and demonstration of a multijunction module which exhibits 8.8% efficiency after 600 hours degradationn at 50°C under AM1.5 global illumination. Subordinate objectives include the selection of the submodule design, characterization and elimination of defects, the assessment of multijunction module performance as a function of insolation conditions and the development of a cost model.

4.2 SUBMODULE DESIGN

The submodules used for this task will employ light absorbing layers consisting of a-Si-based alloys, deposited by plasma-enhanced CVD on a glass superstrate. In order to limit the power loss arising from the series resistance of the CTO used as the transparent contact, the submodule is constructed as a series monolithically interconnected cells. The isolation of adjacent cells and the interconnection are formed by laser scribing which enables us to avoid wet chemical processing and reduces the active area loss of the interconnect. To enhance the collection of the weakly absorbed near-infrared light, ITO/Ag has been used as a highly reflective rear contact and the CTO is textured to promote light-trapping. In order to achieve good stability while taking advantage of as much of the solar spectrum as possible, three thin light-absorbing layers (a-Si:H, a-Si:H, and a-SiGe:H) are used in the triple stack cell.

The optimal number of segments to use in the module (≈ 30) was determined using the model of Gupta, et al. (21), to minimize power losses. The losses accounted for are the power loss in the CTO, which decreases as the segments get narrower and the power loss in the "dead" interconnect area, which increases as the segments are made narrower. **Figure 4-1** illustrates this effect and shows how the module performance depends on the number of segments. For this calculation, the CTO sheet resistance was 16.5Ω/square and the dead region between segments was 0.010". We eventually chose to use 26 segments, as the electronics on our Spire simulator could not measure a V_{oc} > 65V.

Staebler-Wronski degradation is the predominate degradation mechanism in a-Si-based solar cells. To guide us in the design of a stable module, we have relied on stability tests performed on small area cells. While the interrelationship between thickness and stability has been well-characterized for single junction cells, the available information is not as detailed for multi-junction cells. Our initial measurements have led us to believe that we should be able to make a "thin" triple-stack

Figure 4-1. The power output of a triple stack module and the major power losses as a function of the number of segments in the module.

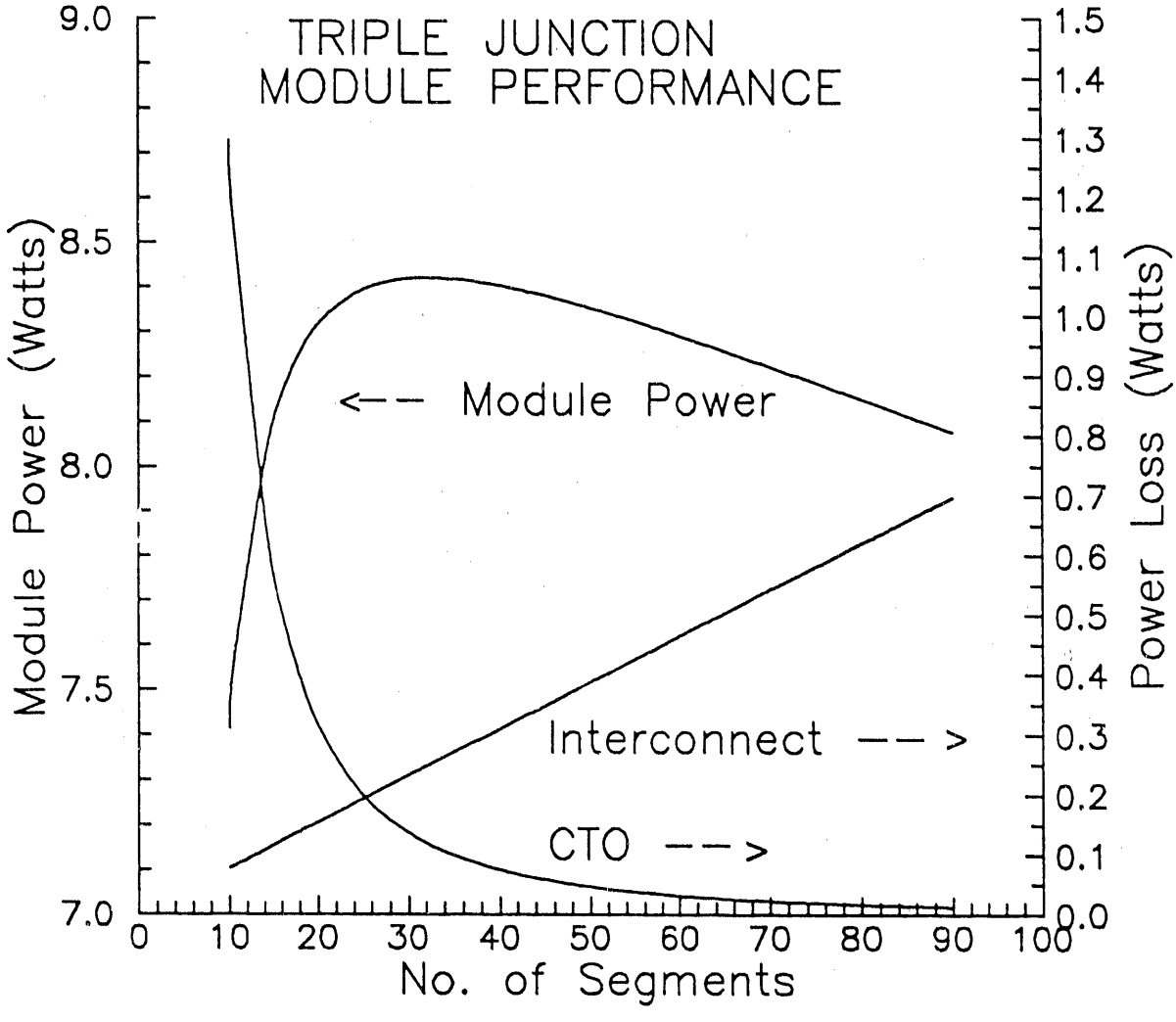

module having a 4000Å thick i_2 layer which will only have a light-induced degradation of about 10%. (The thickness of the i_2 layer, being the thickest light-absorbing layer in the cell, was found to govern the stability of the triple-stack cell.) Since the initial efficiency of the small area triple stack cells with this design is approaching 10%, we believe that our best chance for making a stabilized module will occur using essentially the same design for the light-absorbing layers of the module, assuming that there are no unforeseen instability mechanisms for modules. Having determined the approximate thickness to use for the i_2 layer, convenience has dictated that the initial efficiency be used to measure progress in module development. In later reports, we intend to give more data in terms of results on stabilized modules, particularly if we are able to develop a satisfactory accelerated test.

4.3 PROGRESS TOWARD AN 8.8% STABILIZED MODULE

The best Initial Aperture Area Efficiency (IAPAE) for a triple-stack module having a 6000Å thick i_2 layer, measured at Solarex, is 8.77% (9.27% measured indoors at SERI, 8.25% measured outdoors at SERI). The best module having a 4000Å i_2 layer had an IAPAE of 8.83% measured at Solarex (this module has not been measured by SERI). These modules have ITO/Ag rear contacts, utilize three separate scribes for the CTO, light-absorbing layers, and rear contact, and have closely spaced scribes which increase the active area to 97.7% of the aperture area. The a-Si:H and a-$Si_{1-x}Ge_x$:H materials used in the intrinsic layers are identical to those used for making the best small area triple-stack cells (no microcrystalline layers were used in the recombination layers between the i-layers).

The reduction of the "dead" interconnect area between segments was an important factor in improving the aperture-area performance of our modules. This was accomplished by reducing the power in the laser scribe pulses to the point where each scribe was ≈ .0015" wide. Since we were able to space the scribes ≈ .0025" apart, the total interconnect region was limited to ≈ .010", allowing the achievement of a 97.7% utilization of the aperture area in a 30 segment module.

A few of our modules, fabricated earlier in the Phase I portion of the subcontract, have shown very good indoor stability, consistent with the i_2 thickness dependence seen in small area cells. The modules which had IAPAEs between 6 - 7.5% were not encapsulated and were degraded indoors by exposure to sodium vapor lamps. **Figure 4-2** plots the normalized efficiencies as a function of exposure time for the modules. Although the data clearly shows a higher rate of degradation for the thicker devices, the thinnest triple junction device which had i_2 = 4000Å showed only a 10%

Figure 4-2. Indoor degradation data of triple junction modules (unencapsulated) as a function of time. Modules are referred to by the thickness of the middle junction or i_2 layer. Also shown for comparison is data for an a-Si:H/a-Si:H module with a bottom i-layer thickness of 2500Å.

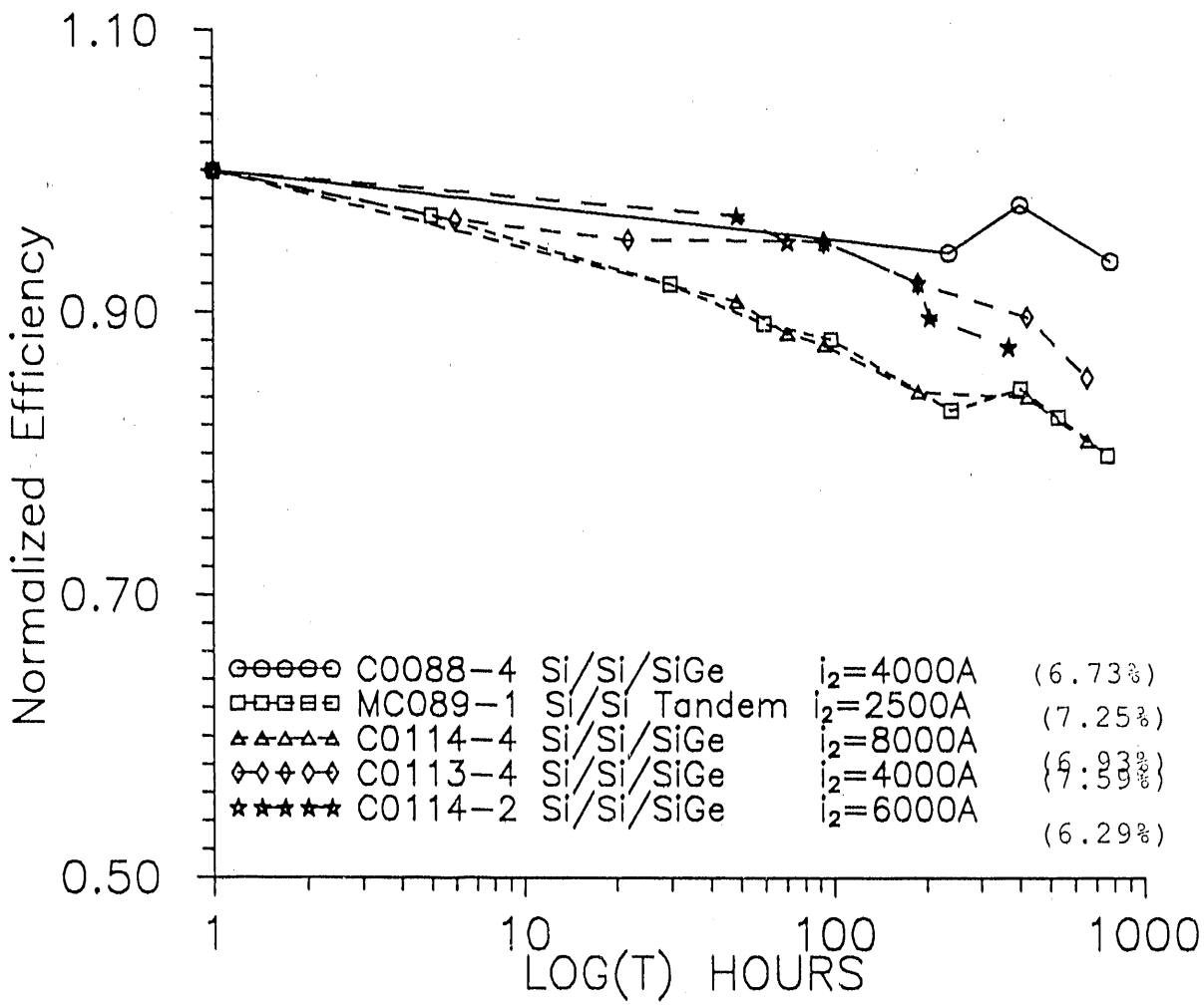

loss after 500 hours. For comparison, a tandem 2500Å (i_2) a-Si:H/a-Si:H module exhibited a loss of 20% after 1000 hours, comparable to the thickest (i_2 = 8000Å) triple junction submodule.

Some of the first encapsulated modules which are being degraded outdoors at V_{oc} show an anomalous degradation, while others are degrading at a rate which is comparable to that seen on encapsulated "daughter" modules which are being degraded indoors. **Figure 4-3** shows stability measurements performed on three nearly identical modules having 6000Å i_2 layers, two of which were degraded outdoors and one was degraded indoors. In this case, the module being degraded indoors is performing marginally better than the modules being degraded outdoors. Indeed, we have generally found that the modules are experiencing either greater losses than that measured for small area cells or early unencapsulated modules. We have also found that the modules do not exhibit the expected dependence of stability on thickness. In **Figure 4-4**, the indoor degradation of three modules having different i_2 layer thicknesses is shown. It might be argued that the increased stability effect for thinner modules is masked when the modules are degraded at V_{oc}, however, the thickness effect was not masked for the small area cells. We also find that some modules, which have a low shunt resistance, experience a loss in V_{oc} after light-soaking which is greater than expected.

In any event, the results should be viewed as preliminary since relatively few modules have been light-soaked and further advances in reducing the shunt problem may have a significant impact on stability.

4.4 DEFECTS AND UNIFORMITY OF MODULES

The most stubborn problem which has been encountered in the fabrication of the "thin" modules is the avoidance of the shunt along the laser scribe of the rear contact. The shunt was discovered to result from crystallization of the a-Si-based layers in the heat-affected zone along the edges of the scribe. We found that lowering the energy per pulse of the Q-switched Nd-YAG laser to $\approx$ 30 μJ played a large role in reducing the size of the heat-affected zone and the concurrent shunt. By this method, the segment-to-segment leakage current, measured at -4V reverse bias, is often reduced to < 10 mA. The source of the shunt which is responsible for the remainder of the leakage current may not be related to the laser scribe, as significant leakage can sometimes be found in large area cells which do not contain any laser scribes. We have not yet completed the study of the influence of the scribe quality on module performance and stability. A significant portion of our time over the next six months is expected to be expended on these

Figure 4-3. Comparison of the indoor and outdoor stability measurements of encapsulated triple-stack modules.

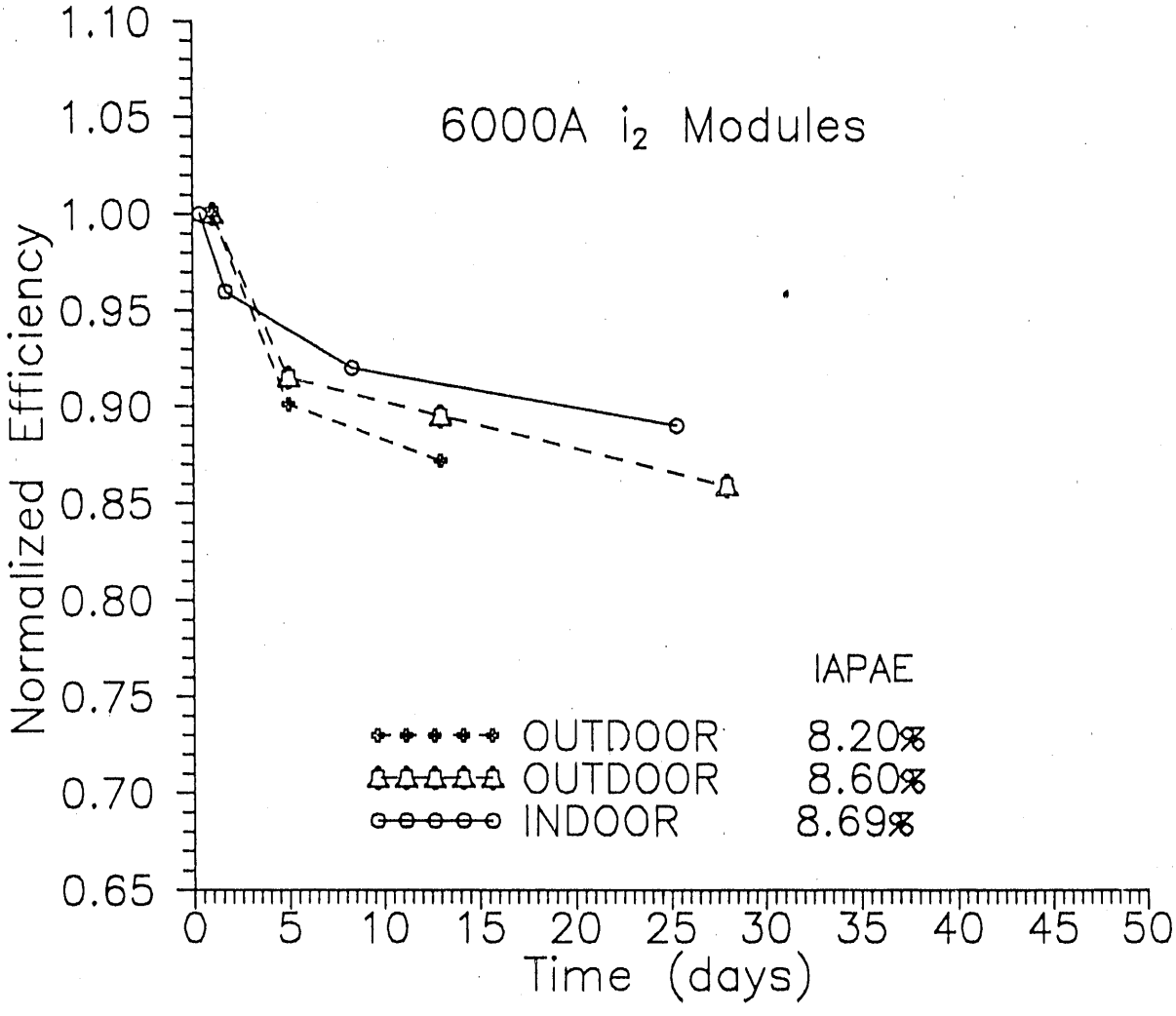

Figure 4-4. The indoor degradation of modules having different i_2 layer thicknesses.

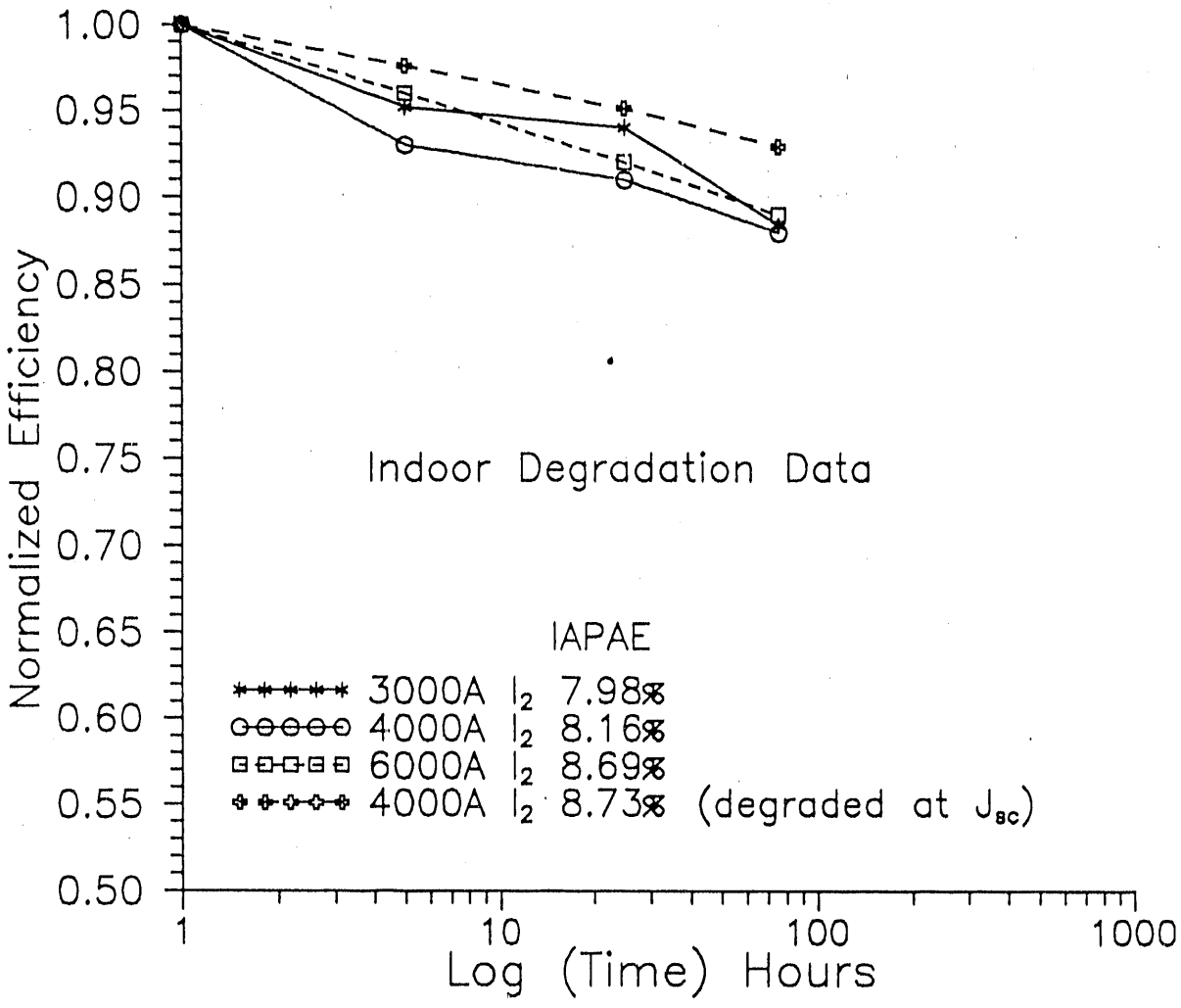

issues, as improvements in these areas will have a direct impact on the stabilized module efficiency. We also expect that a further reduction in the number of point defects will allow us to make thinner triples if these are deemed necessary to achieve the requisite stability.

Good uniformity is necessary to insure the maximum performance of large area photovoltaic modules. We have developed a simple procedure for testing the uniformity of a 12"x13" module. A series of 17 evenly spaced laser scribes are made perpendicular to the original interconnect scribe. An Oriel simulator with a computer-controlled x-y table is used to automatically measure I-V curves for the 442 cells which are formed on the 12" x 13" substrate. **Figure 4-5** shows how J_{sc} varies over a typical module. A large part of this variation is believed to arise from non-uniformities in the a-SiGe:H layer. The impact of the non-uniformity in the CTO sheet rho and haze (see **Table 4-1** below) are also being investigated to assess their impact on module performance. The measurement of haze, defined as the ratio of the diffuse optical transmittance to the total transmittance, has been found to be a convenient method of characterizing the light-scattering ability of CTO.

Table 4-1

The Variation in CTO Haze and Uniformity over a 12"x13" Substrate

CTO Uniformity			
Haze			
33.2	32.3	34.9	32.9
22.8	20.2	21.9	22.4
20.7	18.6	19.4	20.9
31.8	29.4	30.9	31.9
Sheet Rho (Ohms/Square)			
13.8	13.8	14.0	13.0
16.7	16.7	16.1	16.1
18.0	19.2	18.6	18.1
14.8	15.7	15.2	15.5

Figure 4-5. The variation in J_{sc} over a 12" x 13" module.

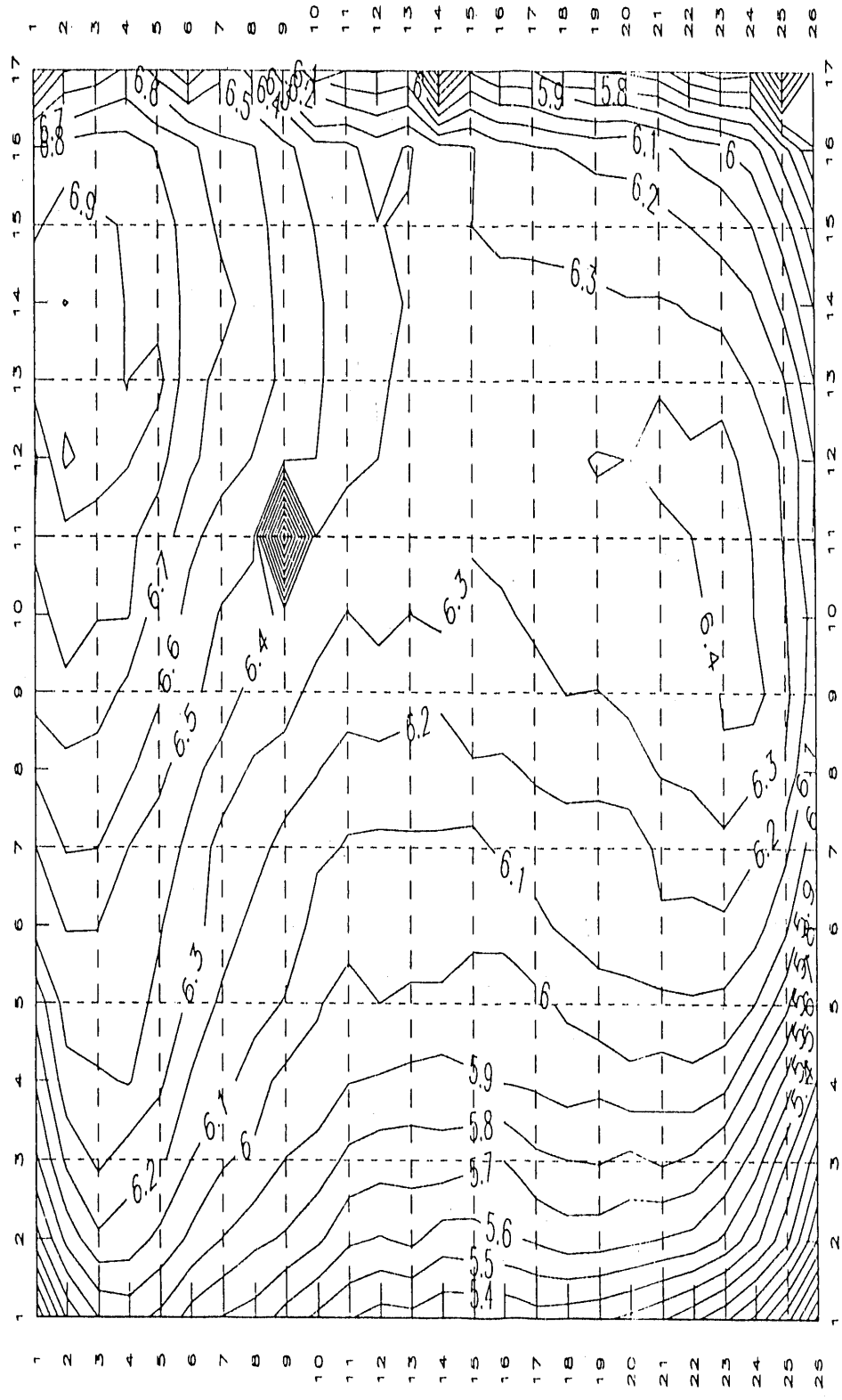

4.5 OPTICAL MODELING OF TRIPLE STACKED CELLS

The Solarex optical model was used to project the maximum current density which should be achievable using the present structure of glass/CTO/p-i-n(a-Si)/p-i-n(a-Si)/p-i-n(a-SiGe) /ITO/Ag. It is desirable to know not only the maximum J_{sc} which could be expected if all losses in the doped layers were eliminated, but also the intrinsic layer thicknesses required to produce that J_{sc}. It is also important to know the origin and magnitude of optical losses other than those due to doped layer absorption.

The J_{sc} of this triple structure will be limited by the first two junctions, because 1.7 eV a-Si:H limited long wavelength photoresponse. Early optical modeling confirmed that the first three doped layers (p_1 layer and first tunnel junction layers) most greatly influence optical loss of the cell. In the limiting case of no optical losses in the first three (p_1, n_1, p_2) doped layers of the triple, and assuming a second intrinsic layer thickness limited to 7000Å, an 85% peak response with 7.8 mA/cm^2 would be expected for complete photocollection (**Figure 4-6**). This accounts for all other optical losses typical of this structure, including rear contact and CTO absorptive losses, and reflection losses (no front AR coating is assumed also). Upon introduction of practical thicknesses for doped layers the maximum J_{sc} is reduced. The maximum J_{sc} expected based on combinations of the following thicknesses of layers (in Angstroms) in a triple cell is shown in **Table 4-2** below.

Table 4-2

Projected J_{sc} of Triple Junction Cells as a Function of i-Layer Thickness Assuming No Improvement in Front Contact or Doped Layers

P_1	I_1	N_1	P_2	I_2	J_{sc} (Maximum)
100	490	60	100	4300	6.5 mA/cm^2
100	570	60	100	6000	7.0 mA/cm^2
100	600	60	100	7000	7.2 mA/cm^2

Figure 4-6. Expected quantum efficiency for the limiting case of no optical losses due to doped layers preceding the second intrinsic layer, complete collection is also assumed. The major losses due to non-semiconductor materials, using present technology, are also shown.

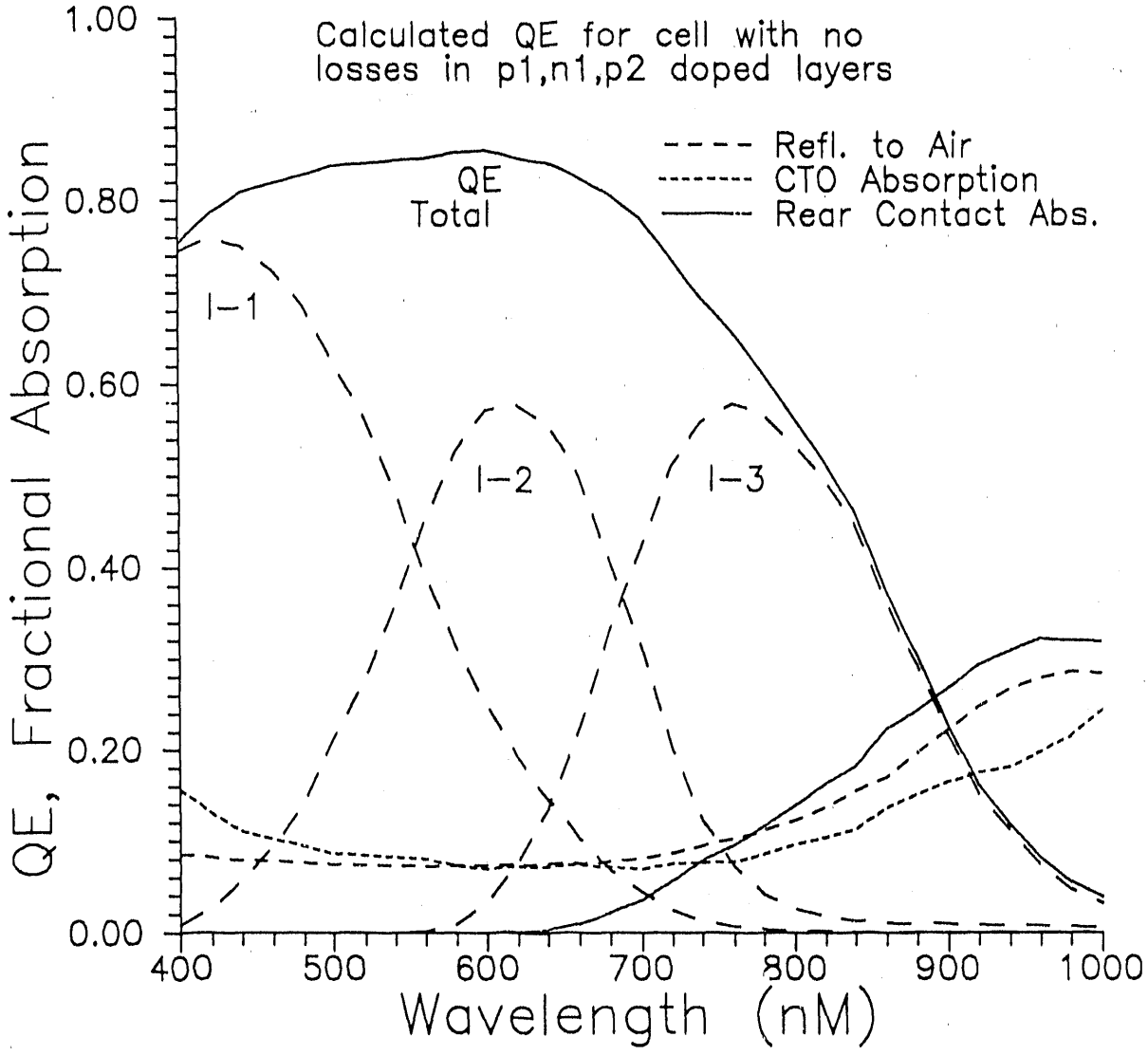

Practical triple structures using i_2 a-Si thicknesses of 6000Å have yielded J_{sc}'s which are approaching that predicted above (**Figure 4-7**). One discrepancy, however, is that in practice a slightly different thickness of I_1 layer is required than is predicted above to balance current generation in each of the junctions. This is probably because the distribution of interfacial scattering which is assumed in the optical model (Lambertian) is not exactly representative of the scattering which actually takes place.

Efforts to improve the triple structure with respect to doped layer absorption have centered around optimizing the thickness and doping concentrations of these layers. This process is complicated by the strong dependence of V_{oc} and fill factor on these variables.

Modeling has indicated that the major optical losses in non-a-Si:H layers are confined to three mechanisms; absorptive loss in the front CTO contact, absorptive loss at the rear contact, and reflective loss which eventually returns optical energy to the ambient. The approximate optical absorption in the most important (non-semiconductor) layers of a triple stack cell of typical design, using present technology, are shown in **Table 4-3** below.

Table 4-3

Triple Cell Optical Absorption (In Terms of mA/cm^2)	
Reflection to Air	4 mA/cm^2
CTO Absorption	4 mA/cm^2
Rear Contact Absorption	4 mA/cm^2
Actual Collected J_{sc} in Intrinsic Layers (assuming 6.6 mA/cm^2/junction)	20 mA/cm^2
(Sub-total)	32 mA/cm^2
Total Available in AM1.5 Global Spectrum (400 to 1000 nm Wavelengths)	38 mA/cm^2

Figure 4-7. Quantum efficiency of an actual triple stack cell having a 6000Å I-2 layer. Due to improvement in doped layers, the QE currents collected in the intrinsic layers approach those predicted by the optical model for this type of cell.

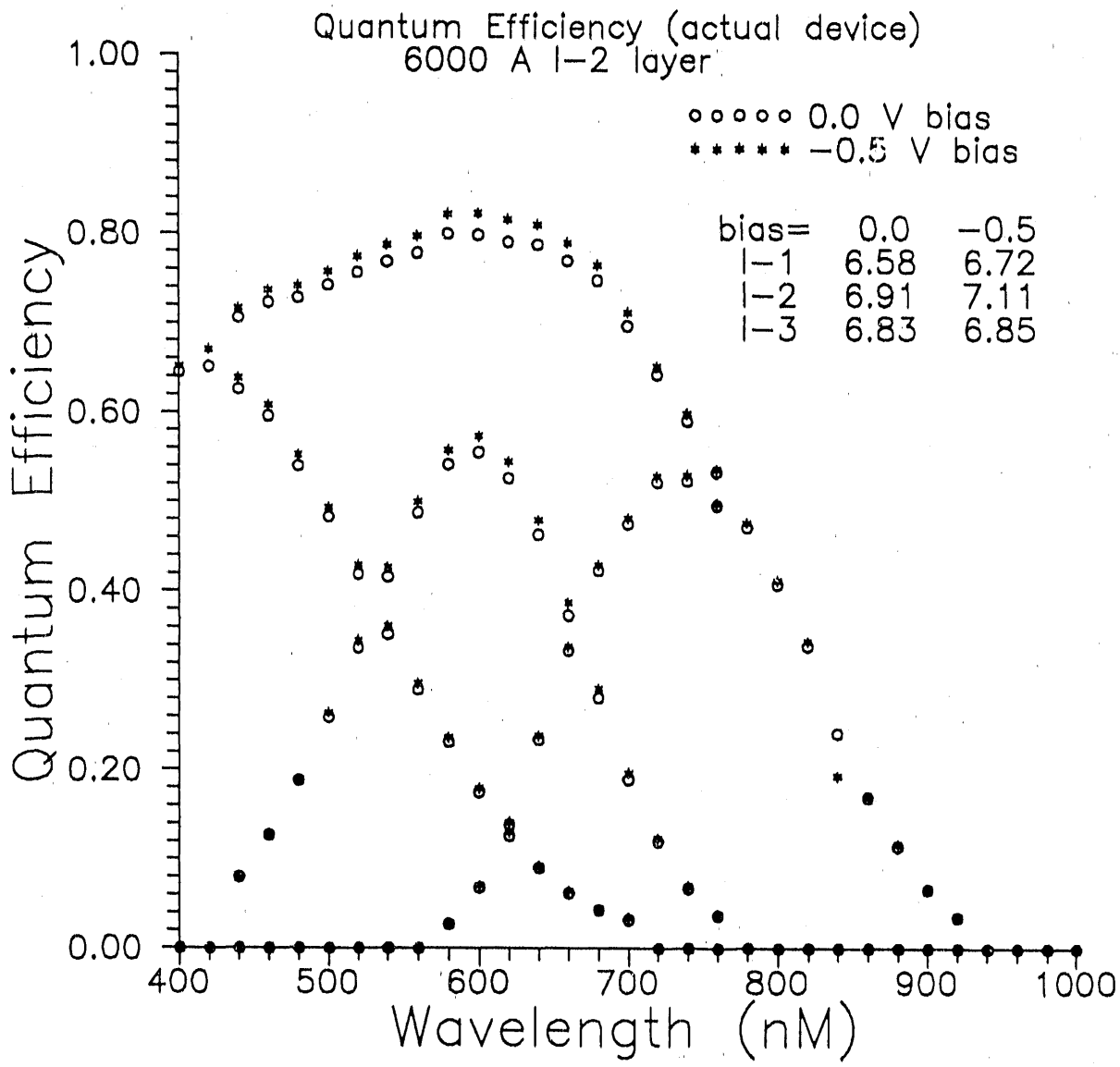

The multitude of remaining smaller optical losses, such as residual absorptive losses in the doped layers, ITO interface layer at the rear contact, tunnel layers and glass, along with collection losses in the i-layers themselves together account for the remaining 6 mA/cm^2. This analysis indicates that the effort toward reducing optical losses should be directed specifically to improve the front CTO characteristics and the rear contact characteristics further. Some preliminary investigation has begun to further increase the reflectivity of the ITO/Ag rear contact which is presently used.

4.6 IMPROVEMENTS IN THE RECOMBINATION LAYER (TUNNEL JUNCTION)

At one time we expected that an improvement in solar cell performance could result from an improvement in the recombination in the "tunnel junction" between adjoining semiconductor layers in a triple stack cell. However, we have been able to make small area devices with good fill factors (≥ .72) using any of the following layers in the tunnel junction: 1) microcrystalline doped layers, 2) a-SiC:H doped layers, or 3) a-Si:H doped layers.

At the present time, no further experiments are planned concerning the tunnel junction as it does not appear to be limiting module performance.

4.7 OTHER SUBTASK RESEARCH ACTIVITIES

The assessment of the performance of multijunction modules as a function of temperature, solar spectrum, intensity, etc. has not yet been addressed, nor have the cost and manufacturability issues been addressed.

REFERENCES

1. W.A. Turner, S.J. Jones, D. Pang, B.F. Bateman, J.H. Chen, Y.-M. Li, F.C. Marques, A.E. Wetsel, P. Wickboldt, W. Paul, J. Bodart, R.E. Norberg, I. ElZawawi, M.L. Theye, J. Appl. Phys. 67, 7430 (1990).
2. Final Subcontract Report for Period 1 February 1989 - 28 February 1990, Contract No. ZB-7-06003-2, Report No. SERI/TP-211-3906, Solarex Thin Film Division.
3. L. Yang, J. Newton, B. Fieselmann, Mat. Res. Soc. Symp. Proc., Vol. 149 (MRS, Pittsburgh, 1989), p. 497.
4. K.D. MacKenzie, J.R. Eggert, D.J. Leopold, Y.M. Li, S. Lin, W. Paul, Phys. Rev. B31 (1985), p. 2198.
5. H. Fritsche, in *Semiconductors and Semimetal*, Vol. 21, part C, edited by J. Pankove, Academic Press, Orlando, 1984, p. 309 and references therein.
6. D. Ritter, K. Weiser, E. Zeldov, J. Appl. Phys., 62, 4563 (1987).

7. L. Yang, A. Catalano, R. Arya, M. Bennett, I. Balberg, MRS Symp. Proc. Vol. 149, 563, 1989.

8. I. Balberg, A.E. Delahoy, H.A. Weakliem, Appl. Phys. Lett. 53, 992 (1988).

9. C.R. Wronski, R.E. Daniel, Phys. Rev. B23, 794 (1981).

10. A. Many, Y. Goldstein, N.B. Grover, *Semiconductor Surface*, North Holland, New York, 1971.

11. R.W. Collins, in *Amorphous Silicon and Related Materials*, Vol. B, edited by H. Fritsche, World Scientific, Singapore, 1989, p. 1003.

12. A. Catalano, M. Bennett, R.R. Arya, K. Rajan, J. Newton, Proceedings of the 18th IEEE Photovoltaic Specialists Conference (IEEE, N.Y., 1985), p. 1378.

13. M. Bennett, K. Rajan, Proceedings of the 20th IEEE Photovoltaic Specialists Conference (IEEE, N.Y., 1988), pp. 67-72.

14. S.J. Fonash, R. Kakkad, private communication.

15. C. Kittell, "Introduction to Solid State Physics", 5th ed., John Wiley & Sons, 1976, p. 210.

16. R.G. Gordon, et al., Solar Energy Materials, Vol. 18, 1989, p. 263.

17. R.E.I. Shropp, A. Madan, J. Appl. Phys., Vol. 66, 1989, p. 2027.

18. P.S. Vijayakumar, et al., U.S. Patent 4,751,149 (1988).

19. J. Shealy, et al., J. Electrochem. Soc., Vol. 128, 1981, p. 558.

20. C.K. Lau, et al., J. Electrochem. Soc., Vol. 127, 1980, p. 1843.

21. Y. Gupta, H. Liers, S. Woods, S. Young, R. DeBlasio, L. Mrig, Proceedings of the 16th IEEE Photovoltaic Specialists Conference (IEEE, N.Y., 1982).

Document Control Page	1. SERI Report No. SERI/TP-214-4271	2. NTIS Accession No. DE91002138	3. Recipient's Accession No.

4. Title and Subtitle

Research on Stable, High Efficiency Amorphous Silicon Multijunction Modules

5. Publication Date
April 1991

6.

7. Author(s)
A. Catalano, R. Arya, M. Bennett, B. Fieselmann, Y. Li, J. Morris, J. Newton, R. Podlesny, S. Wiedeman, L. Yang

8. Performing Organization Rept. No.

9. Performing Organization Name and Address

Solarex Thin Film Division
826 Newtown-Yardley Road
Newtown, Pennsylvania 18940

10. Project/Task/Work Unit No.
PV140201

11. Contract (C) or Grant (G) No.

(C) ZM-0-19033-1

(G)

12. Sponsoring Organization Name and Address
Solar Energy Research Institute
1617 Cole Blvd.
Golden, CO 80401

13. Type of Report & Period Covered
Technical report

14.

15. Supplementary Notes
SERI technical monitor: W. Luft, (303) 231-1823

16. Abstract (Limit: 200 words)

This research effort seeks to develop modules with a stabilized performance of 8.8% aperture area conversion efficiency after 600 hours light exposure (AM1.5) at 50°C in modules with aperture areas over 900 cm^2. Good progress toward this goal has been obtained with the demonstration of 9.3% initial performance in a submodule incorporating devices with relatively thin middle junction i-layer thickness of 600Å. Devices with this design are expected to lose about 15% of their initial performance after 1000 hours of exposure.

Achieving long-term stabilized efficiencies of 12% or more requires substantial improvements in materials and devices. Our analysis has shown that substantial optical losses occur at both front and rear contacts which we hope to address with ZnO films prepared by CVD and sputtering processes now under development. Further progress in doped layers and alloys are also needed. Fundamental studies of the relationship between material structure and processes (particularly the effect of hydrogen dilution) are reported here.

17. Document Analysis
a. Descriptors
photovoltaics ; solar cells ; amorphous silicon ; thin film ; multijunction modules

b. Identifiers/Open-Ended Terms

c. UC Categories
271

18. Availability Statement
National Technical Information Service
U.S. Department of Commerce
5285 Port Royal Road
Springfield, VA 22161

19. No. of Pages
68

20. Price
A04